AUTHOR QUERY FORM

ELSEVIER	**Journal:** CCR	**Please e-mail your responses and any corrections to:**
	Article Number: 112053	**E-mail:** corrections.esch@elsevier.thomsondigital.com

Dear Author,

Please check your proof carefully and mark all corrections at the appropriate place in the proof (e.g., by using on-screen annotation in the PDF file) or compile them in a separate list. Note: if you opt to annotate the file with software other than Adobe Reader then please also highlight the appropriate place in the PDF file. To ensure fast publication of your paper please return your corrections within 48 hours.

For correction or revision of any artwork, please consult http://www.elsevier.com/artworkinstructions.

Any queries or remarks that have arisen during the processing of your manuscript are listed below and highlighted by flags in the proof. Click on the 'Q' link to go to the location in the proof.

Location in article	Query / Remark: **click on the Q link to go** **Please insert your reply or correction at the corresponding line in the proof**
Q1	Please confirm that given names and surnames have been identified correctly.
Q2	The symbol '*' has been removed from the authors "Danilo Dini and Elizabeth A. Gibson", since it has no significance. Please check, and correct if necessary.
Q3	Please check whether the designated corresponding author and telephone/fax number are correct, and amend if necessary.
Q4	Please check the edit(s) made in the "Highlights", and correct if necessary.
Q5	Please check the hierarchy of the section headings.
Q6	"Your article is registered as belonging to the Special Issue/Collection entitled "COST-Jena; by invitation". If this is NOT correct and your article is a regular item or belongs to a different Special Issue please contact s.shanmugam@elsevier.com immediately prior to returning your corrections.".
Q7	Please check the placement of Table 2, and correct if necessary.
Q8	Please check the placement of Fig. 19, and correct if necessary.
Q9	Please note that Refs. [13,89] and [54,121] were identical, and Ref. [89,121] have been deleted. The subsequent references have been renumbered.
Q10	Part label (c) is mentioned in the caption of Fig. 15 but it is not provided in artwork. Please check.

Please check this box or indicate your approval if you have no corrections to make to the PDF file	

Thank you for your assistance.

Graphical Abstract

The influence of the preparation method of NiO$_x$ photocathodes on the efficiency of p-type dye-sensitized solar cells

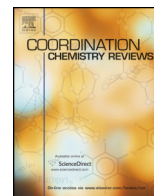Danilo Dini, Yvonne Halpin, Johannes G. Vos*, Elizabeth A. Gibson

A range of preparation methods for p-type NiO electrodes are reported together with associated DSC cell parameters and electrochemical details.

Highlights

The influence of the preparation method of NiO$_x$ photocathodes on the efficiency of p-type dye-sensitized solar cells

Coordination Chemistry Reviews xxx (2015) pp. xxx–xxx

Danilo Dini, Yvonne Halpin, Johannes G. Vos[*], Elizabeth A. Gibson

Q4

- Discussion of effect of preparation method of NiO thin layers on the structural features of NiO modified electrodes.
- Discussion of effect of preparation method of NiO thin layers on their DSC parameters.
- Discussion of effect of preparation method of NiO thin layers on the electrochemical properties.
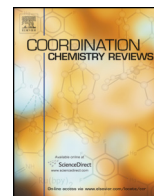
Review

The influence of the preparation method of NiO$_x$ photocathodes on the efficiency of p-type dye-sensitized solar cells

Q1 Danilo Dini[a], Yvonne Halpin[b], Johannes G. Vos[b,*], Elizabeth A. Gibson[c]

[a] Department of Chemistry, University of Rome "La Sapienza", Rome, Italy
[b] SRC for Solar Energy Conversion, School of Chemical Sciences, Dublin City University, Dublin 9, Ireland
Q2 [c] School of Chemistry, Newcastle University, Newcastle upon Tyne NE1 7RU, UK

Contents

ABSTRACT

Improving the efficiency of p-type dye-sensitized solar cells (DSCs) is an important part of the development of high performance tandem DSCs. The optimization of the conversion efficiency of p-DSCs could make a considerable contribution in the improvement of solar cells at a molecular level. Nickel oxide is the most widely used material in p-DSCs, due to its ease of preparation, chemical and structural stability, and electrical properties. However, improvement of the quality and conductivity of NiO based photocathodes needs to be achieved to bring further improvements to the solar cell efficiency. The subject of this review is to consider the effect of the preparation of NiO surfaces on their efficiency as photocathodes.

© 2015 Elsevier B.V. All rights reserved.

Q5 ## 1. Introduction

Q6 Over the past couple of decades dye-sensitized solar cells (DSCs) have received increasing attention as an alternative to traditional crystalline silicon based photovoltaic devices. Dye sensitized solar cells are significantly cheaper to produce than crystalline silicon devices but are less efficient. A proposed way to improve the photo-conversion efficiency of these devices above 15% is to pair a conventional TiO$_2$-based photoanode with a photocathode based on a dye-sensitized mesoporous p-type semiconductor in a tandem device, Fig. 1 [1–4].

Since the first tandem cell containing a dye-sensitized photoanode and dye-sensitized photocathode in a single device was reported by He et al. [1] in 2000, improvements to the NiO have been translated to an increase in tandem cell efficiency. The tandem DSC assembled from an erythrosine B-sensitized NiO cathode and a N3-sensitized TiO$_2$ anode gave a V_{OC} = 732 mV, approximately the sum of the V_{OC} values from the n-type device (650 mV) and the p-type device (83 mV). The overall efficiency, 0.39%, was low because of the low current on the p-side. Suzuki et al. [4] prepared a tandem device with their P123-templated NiO and a N3-sensitized TiO$_2$ anode (also prepared using P123) which gave an efficiency of 0.78% when illuminated through the cathode. As for the device prepared by He et al., there was a mismatch in the J_{SC} of the two electrodes and so the fill factor was extremely low. Improvements to the J_{SC} brought about by improvements to the dye and in NiO substrate have since enabled a tandem cell to be assembled where the cathodic and anodic photocurrents were matched (improved fill factor of 0.74). The open-circuit voltage (V_{OC}) of 1079 mV, the highest ever reported for electrolyte-based photoelectrochemical solar cells, closely matched the sum of V_{OC} for n-DSC and p-DSC. The efficiency of a cell illuminated through the cathode was 2.42%

Q3 * Corresponding author. Tel.: +353 1 7005307; fax: +353 1 7005503.
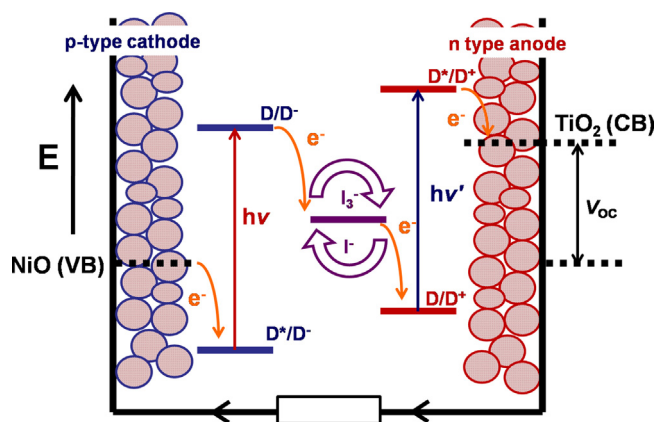E-mail address: Han.Vos@dcu.ie (J.G. Vos).

Fig. 1. A schematic illustration of a tandem-DSC where a n-type photoanode and a p-type photocathode are incorporated into a single device. In these solar cells the photovoltage arises from the difference in the quasi-Fermi levels close to the conduction band (CB) edge of the photoanode and at the valence band (VB) edge of the photocathode (approximately the sum of the photovoltages obtained with the individual devices).

Fig. 2. Schematic illustration of the operating principle behind a p-DSC. (1) Represents the difference in potential between the Fermi level of the NiO and the redox couple, which is the maximum photovoltage of the device. (2) and (3) represent recombination processes between the redox couple and the NiO (2) and the photoreduced dye and the NiO (3).

and a cell illuminated through the anode was 1.91% compared to 13% for n-DSCs obtained by Grätzel et al. [5]. New and improved dyes for p-DSCs are reported frequently and improvements to the spectral response in the red region is enabling higher photocurrents to be obtained in p-DSCs ($8.21\,\mathrm{mA\,cm^{-2}}$) and tandem devices ($5.15\,\mathrm{mA\,cm^{-2}}$) [6].

Further improvements to the material, including finding an alternative p-type semiconductor, and understanding of the charge-recombination processes which limit the efficiency are needed if target efficiencies exceeding 15% are to be met.

The poor performance of the p-type device is attributed to the low photocurrent of the photocathode component. Improving the efficiency of p-type DSCs is essential to the development of high performance tandem DSCs. Compared to the enormous amount of work dedicated to improving the Grätzel type n-DSCs, far less attention has been paid to p-type dye-sensitized solar cells (p-DSC) until recently. The maximum photo-conversion efficiency of p-DSC that has been reached so far is 1.3% [7], substantially limiting tandem cell efficiencies. The optimization of the conversion efficiency of p-DSCs could make a step-change in the efficiency of solar cells that function at a molecular level.

Unlike conventional PV devices, light absorption and charge transport are performed by separate materials in DSCs. The operation principle of a p-DSC is illustrated in Fig. 2. Light excitation of the dye (D) leads to the formation of its excited state (D*) which decays by charge transfer from the valence band of the NiO to form the charge separated state $D^-/NiO(h^+)$. As with charge separation in n-type devices, this can occur on short timescales (0.2–200 ps) [8]. The holes (h^+) diffuse through the NiO to a back contact, which is typically glass coated with fluorine doped tin oxide (FTO). A redox shuttle (typically I_3^-/I^- to match the best n-DSCs) then accepts an electron from the reduced dye (D^-) to restore D and transport the electron to the counter electrode where it is delivered into the external electric circuit. The relative rates of these elementary processes control the efficiency of each step and have therefore a direct impact on the overall efficiency of the cell. The choice of sensitizer is key to maximizing the power output of DSC devices. The dye used on the photocathode should absorb light in the red region of the visible spectrum. This will minimize spectral overlap with the higher energy absorbing dyes on the TiO$_2$ photoanode. n-Type DSCs have been optimized with dyes that absorb between 400 and 600 nm, therefore under working conditions the photocathode would be at the underside of the tandem device and therefore would be required to absorb at longer wavelengths, which are not
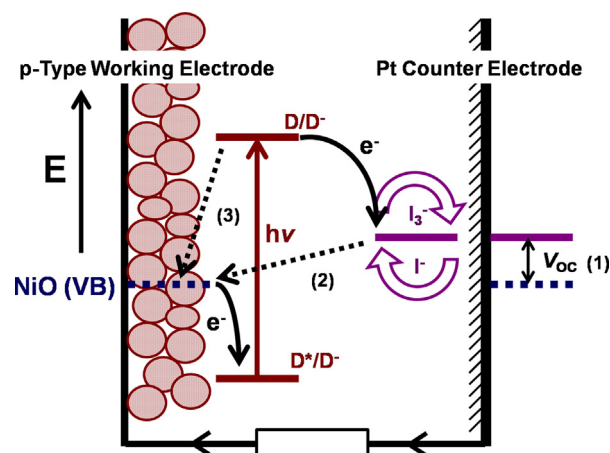
absorbed. Discussion of the dyes is outside the scope of this review [4,7,9–11] but the structures of some of the most widely used or best performing molecules are given in Fig. 3.

IPCE (incident photon-to-current efficiency) experiments, also known as the external quantum efficiency, examine how efficiently the device converts incident photons of monochromatic light into short-circuit current, Eq. (1). Where J_{SC} is the short-circuit current, φ is the quantum yield, LHE is the light harvesting efficiency, η_{inj} is efficiency of charge injection at the dye-semiconductor interface and η_{coll} is the efficiency of charge collection at the SnO$_2$:F contact

$$\mathrm{IPCE} = J_{SC}(\lambda)/e \cdot \phi(\lambda) = \mathrm{LHE}\,\eta_{inj}\eta_{coll} \tag{1}$$

From this we can also calculate the APCE (absorbed photon-to-current efficiency), also known as the internal quantum efficiency. This gives how efficiently a device converts absorbed photons into current. APCEs are calculated by Eq. (2)

$$\mathrm{APCE} = \frac{\mathrm{IPCE}}{\mathrm{LHE}} \tag{2}$$

This is very useful for comparing dyes as not all will have the same dye loading onto the NiO-semiconductor. LHE can be determined by the absorbance of the electrode, A, at λ_{max}, Eq. (3):

$$\mathrm{LHE} = 1 - 10^{-A} \tag{3}$$

Improving the quality of the material, thereby improving the η_{coll} is thus a key challenge in the field.

The power conversion efficiency of a solar cell (η) is the product of three terms, which are the short circuit photocurrent density (J_{SC}), the open-circuit photovoltage (V_{OC}) and the fill factor (ff) divided by the incoming incident solar power (P_{in}, $100\,\mathrm{mW\,cm^{-2}}$ for all devices mentioned in this review unless stated) according the Eq. (4):

$$\eta = \frac{P_{max}}{P_{in}} = \frac{J_{SC} \cdot V_{OC} \cdot \mathrm{ff}}{P_{in}} \tag{4}$$

Maximizing any of these terms increase η. If one takes the usual values of these three factors, we observe that all of them are relatively very low compared to those of a conventional n-DSC. The best NiO p-DSC with I_3^-/I^- electrolyte exhibits $J_{SC} = 7.0\,\mathrm{mA\,cm^{-2}}$, $V_{OC} = 185\,\mathrm{mV}$ and ff = 0.33 which gives a η of 0.43% [12], while standard TiO$_2$ based n-DSSCs classically display about 8–10% efficiency with typical values of $J_{SC} = 18\,\mathrm{mA\,cm^{-2}}$, $V_{OC} = 700\,\mathrm{mV}$ and ff = 0.70 [13]. Evidently the choice of semiconductor has an enormous impact on the device efficiency and to bring the
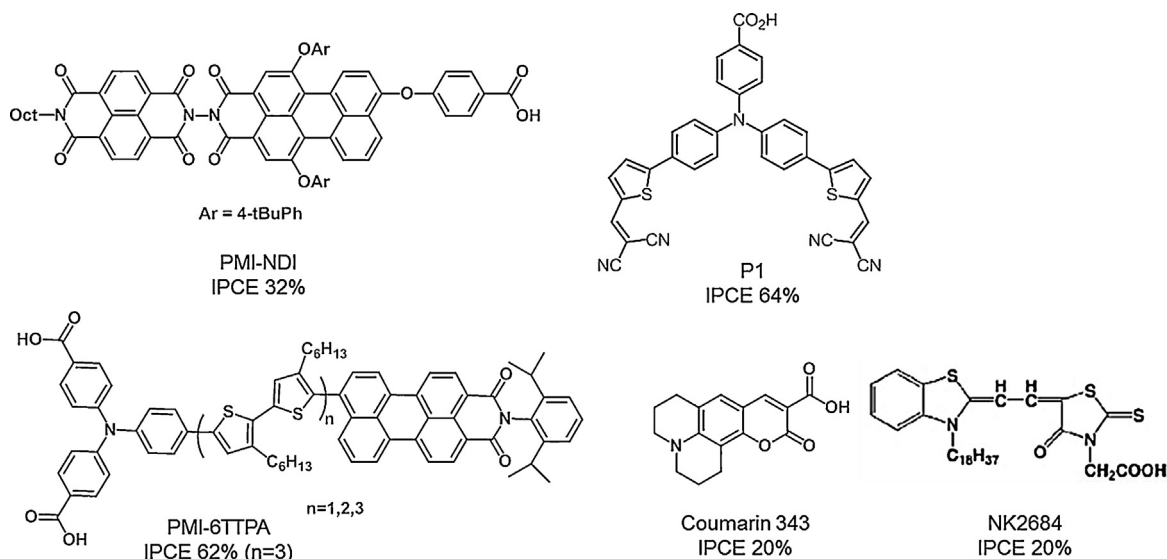
Fig. 3. Structures of some of the best performing dyes used in NiO p-DSCs with their maximum incident photon-to-current conversion efficiencies (IPCE).

performance of p-DSCs up to that of n-DSCs much work is required to understand and develop the semiconductor material.

The subject of this review is the impact of the nature of NiO on the device efficiency. NiO is the most widely used material in p-DSCs, due to its ease of preparation. However, a number of improvements to the quality and conductivity of the material need to be addressed in order to bring increase solar cell efficiency. So far attempts to improve the efficiency of NiO-based photocathodes have mainly concentrated on varying the dyes [6,14]. In these studies parameters such as the absorption properties and the related molar absorption coefficients have been considered. However, less attention has been paid to the effect that the preparation method of the NiO electrodes may have on their photovoltaic behaviour. This is surprising since it is to be expected that the structural features of the NiO films, such as morphology and porosity, will greatly affect cell behaviour, since they will control at least partly the charge transport through the modifying NiO to the conducting substrate. It is well established that while the overall electrochemistry of NiO layers does not vary greatly with the morphology of the layer, kinetic parameters such as charge transport do.

Therefore, a range of approaches for the preparation of thin NiO layers are discussed. The cell performance parameters of the resulting photovoltaic cells are compared where possible, while the light induced charge lifetimes and diffusion lengths observed within the layers are also considered. In addition a section outlining the effect of the film structure on the electrochemical parameters of coated and uncoated NiO electrodes is considered. An overview of this analysis is shown in Table 1. In this table the cell preparation and the performance parameters of the various designs discussed in this review are listed together with those for some other related systems [15–22].

2. Electrode preparation and solar cell performance parameters

In the first p-type and tandem DSCs demonstrated, He et al. [1,23] prepared the electrodes by spreading a Ni(OH)$_2$ slurry using a glass rod ("doctor blade") onto SnO$_2$:F (FTO) conducting glass substrates and sintering in a hot air stream to give porous, nano-structured (20 nm particles) NiO films (Fig. 4). Under illumination erythrosin B and tetrakis(4-carboxyphenyl)porphyrin (TPPC) sensitized NiO films generated a cathodic current. Sandwich cells prepared by assembling the sensitized electrodes with a platinum

foil counter electrode and using a J_3^-/I^- electrolyte solution (ca. 0.44 V vs. NHE) gave a J_{SC} = 0.079 mA cm^{-2} and V_{OC} = 98.5 mV, TPPC cell, and a J_{SC} = 0.232 mA cm^{-2}, V_{OC} = 82.8 mV for the erythrosin B cell when illuminated with sun-simulated light at 68 mW cm^{-2}. The V_{OC} was limited by the small potential energy difference between the NiO valence band and the redox system (1 in Fig. 2), and the current by the low light absorption by the thin film. Films thicker than 1 μm cracked during sintering. The number of dye molecules calculated by the absorbance of the dye in solution and adsorbed on the film was 2.0 × 10^{15} cm^{-2}. This gives an inner area of 300 Å^2/molecule to be compared with an estimated largest molecular area of erythrosin B close to 100 Å^2 [23].

Zhu et al. [24] demonstrated that annealing at 300 °C for 30 min is sufficient to completely convert Ni(OH)$_2$ to NiO using powder X-ray diffraction. From the broadening of the peaks, the average crystal size of NiO calcined at this lower temperature was calculated to be 5.2 nm using the Scherrer equation. In their 2007 paper, the photocurrent and IPCE obtained for p-DSCs using the commercial dye coumarin C343 were slightly higher than those reported earlier by He et al. [23] for NiO sintered at 500 °C and sensitized with erythrosine B.
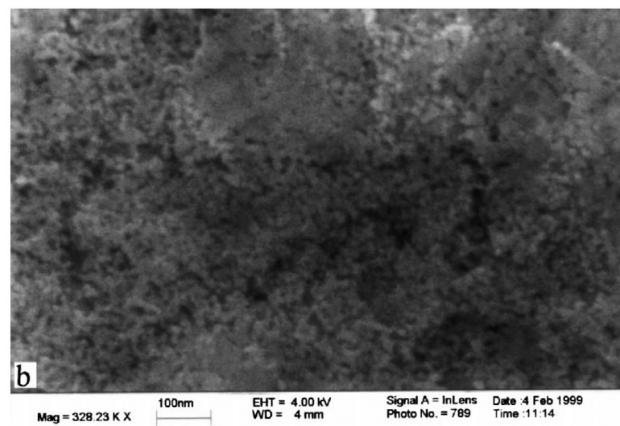

Fig. 4. SEM picture of 1 μm p-NiO film deposited on fluorine-doped SnO$_2$ (FTO) conducting glass.
Reproduced from Ref. [1]. Copyright 2000, with permission from Elsevier.

ARTICLE IN PRESS

Table 1
Summary of the production conditions and performance parameters for p-DSCs.

Ref.	Type	Time (min)	Temp (°C)	Dye	Electrolyte	Film Thickness (μm)	IPCE (%)	J_{SC} (mA cm⁻²)	V_{OC} (mV)	FF	η (%)
Ni(OH)$_2$ sol gel											
[23]		60	500	ERY	0.5 M LiI, 0.05 M I$_2$ EC/PC	1	3.44	0.27	83		
[24]		30	300	c343	0.5 M LiI 0.1 M I$_2$	0.5	6	0.35	80		0.01
[26]		30	300	P1	0.5 M LiI 0.1 M I$_2$ PC	0.6	18	1.52	110	0.31	0.052
[26]		30	300	C343	0.5 M LiI 0.1 M I$_2$ PC	0.6	7.2	0.78	70	0.31	0.017
[22]		30	300	P1	1 M LiI 0.1 M I$_2$ MeCN	1.1–1.4	35	2.5	110	0.29	0.08
[25]		30	450	C343	1.0 M DMII, 0.03 M I$_2$, 0.5 M tbp, 0.1 M GuaSCN, MeCN, VN	1–3		0.48	106	0.33	0.017
Solvothermal Ni(OH)$_2$											
[28]		30	450	C343	0.5 M LiI, 0.1 M I2 PC	3.5		0.66	140	0.38	0.032
[28]		30	350	C343	0.5 M LiI, 0.1 M I$_2$ PC	3.5		0.88	117	0.35	0.036
[30]	"Le Pleux"		350	C343	E-23	15		0.688	124	0.33	0.028
[30]	"improved"		350	C343	E-23	15		1.652	111	0.31	0.056
[15]	Oxalic acid, PVP	30	450	C343	I$_2$, LiI, DMPII, TBP, MPN	1.8	9	0.74	115	0.35	0.03
[31]		120	400	C343	0.6 M DMPII, 0.05 M I$_2$, 0.1 M LiI, 0.5 M TBP, MPN	3		1.95	130	0.36	0.09
Templated sol gel											
[4]	P123	30	450	NK-2684	PN50 Solaronix SA	1		1	93	0.3	0.027
[10]	F88	30	400	C343	0.7 M LiI 0.05 M I$_3^-$ MPN	2.4	21	0.86	101	0.362	0.031
[10]	F88	30	400	fast green	0.7 M LiI 0.05 M I$_3^-$	1.7	14	1.44	93	0.324	0.043
[41]	F88	30	400	NK-2684	0.05 M I$_2$, 0.7 M LiI MeCN	0.5	16	1.2	80	0.35	0.035
[41]	F108	30	400	NK-2684	0.05 M I$_2$, 0.7 M LiI MeCN	0.5	17	1.75	70	0.3	0.035
[41]	F108	30	400	NK-2684	0.05 M I$_2$, 0.7 M LiI MeCN	0.5	17	1.3	80	0.35	0.037
[41]	P105	30	400	NK-2684	0.05 M I$_2$, 0.7 M LiI MeCN	0.5	8	0.6	80	0.35	0.015
[41]	P123	30	400	NK-2684	0.05 M I$_2$, 0.7 M LiI MeCN	0.5	7	0.7	75	0.35	0.017
[9]	F108	30	450	P1	1 M LiI 0.1 M I$_2$	1.2	64	5.48	84	0.37	0.17
[9]	F108	30	450	C343	1 M LiI 0.1 M I$_2$	1.2		1.89	71	0.61	0.08
[16]	F108	30	450	PMI-NDI	1.0 M LiI and 0.1 M I$_2$ PC	2	32	1.76	120	0.345	0.073
[17]	F108	30	450	P1	0.8 M LiI and 0.15 M I2 MeCN	1.5		2.64	104	0.27	0.075

ARTICLE IN PRESS

Table 1 (*Continued*)

Ref.	Type	Time (min)	Temp (°C)	Dye	Electrolyte	Film Thickness (μm)	IPCE (%)	J_{SC} (mA cm^{-2})	V_{OC} (mV)	FF	η (%)
NiO nanoparticles											
[45]	Doctor blade	20	500	C343	0.5 M LiI 0.05 M I$_2$ PC	1.6		0.55	98	0.29	0.016
[45]	Doctor blade	20	500	C343	0.5 M LiI 0.05 M I$_2$ PC	1.6		2.13	37	0.28	0.024
[45]	Doctor blade	20	500	ERY	0.5 M LiI 0.05 M I$_2$ PC	1.6		0.36	77	0.26	0.011
[49]	Screen print			PMI-6TTPA	0.03 M I$_2$, 0.5 M TBP, 0.6 M BMII, 0.1 M GuaSCN, MeCN, VN	2.3	62	5.35	218	0.35	0.41
[51]	Screen print	30 +10	400 550	PMI-6TTPA	0.03 M I$_2$, 0.5 M TBP, 0.6 M BMII, 0.1 M GuaSCN, MeCN, VN	2.7	50	5.11	294	0.41	0.61
[44]	Spray/oven	30	450	ERY	1.0 M LiI, 0.1 M I$_2$ MeCN	0.6		0.353	110	0.35	0.014
[46]	Spray/oven	30	450	P1	1.0 M LiI, 0.1 M I$_2$ MeCN	2.5–3.0	50	2.42	128	0.352	0.11
[46]	Spray/rds	5	450	P1	1.0 M LiI, 0.1 M I$_2$ MeCN	2.5–3.0	44	3.12	103	0.32	0.101
[47]	Spray/rds^A	5	450	ERY	1.0 M LiI, 0.1 M I$_2$ MeCN	2–3		1.05	120	0.36	0.045
[47]	Spray/rds^A	5	450	ERY	1.0 M LiI, 0.1 M I$_2$ MeCN	5–6	11	0.78	100	0.38	0.03
[47]	Spray/rds^B	5	450	ERY	1.0 M LiI, 0.1 M I$_2$ MeCN	3–4	8	1.01	95	0.4	0.039
[47]	Spray/rds^C	5	450	ERY	1.0 M LiI, 0.1 M I$_2$ MeCN	2–3		0.59	110	0.33	0.022
Microballs					2.5–3.0						
[12]	Screen print	30 +10	400 500	PMI-6TTPA	0.03 M I$_2$, 0.5 M TBP, 0.6 M BMII, 0.1 M GuaSCN, MeCN, VN	6	74	7.0	185	0.33	0.43
Hollow spheres											
[20]	Doctor blade	30	450	T1	0.8 M LiI, 0.15 M I$_2$ MeCN	3	30	2.48	159	31.6	0.125
Nanorods											
[53]	SCREEN print	30 +10	400 500	PMI-6TTPA	0.03 M I$_2$, 0.5 M TBP, 0.6 M BMII, 0.1 M GuaSCN, MeCN, VN	1.7	32	3.3	292	0.41	0.4

Table 1 (Continued)

Ref.	Type	Time (min)	Temp (°C)	Dye	Electrolyte	Film Thickness (μm)	IPCE (%)	J_{SC} (mA cm⁻²)	V_{OC} (mV)	FF	η (%)
Insulating Al₂O₃											
[80]	Ni(OH)₂	60	500	WS-PDI	0.15 M I₂, 0.8 M LiI, MeCN	0.3		0.022	61	0.25	3.4 × 10⁻⁴
[80]	Ni(OH)₂ + Al₂O₃	60	500	WS-PDI		0.3		0.025	77	0.24	4.7 × 10⁻⁴
[79]	NiO nanoparticles	30	400			1.3–1.5					
[18]	F108 + ALD Al₂O₃	90	450	P1	0.1 M I₂, 1.0 M LiI, MPN	0.6	11	0.95	150	0.38	0.054
[18]	F108	90	450	P1	0.1 M I₂, 1.0 M LiI, MPN	0.6	8	0.83	110	0.34	0.031
Doped/alloy											
[72]	F108 no Co			O2 dye	0.1 M I₂ 1.0 M LiI, MPN	0.6		0.42	122	0.31	0.016
[72]	F108 6% Co			O2 dye	0.1 M I₂, 1.0 M LiI, MPN	0.6		0.39	158	0.28	0.017
[15]	Oxalic acid, PVP, 1% LiOH	30	450	C343	I₂, LiI, DMPII, TBP, MPN	2	14	0.91	120	0.36	0.039
[19]	"Yarn-ball" + Li		500	C343	0.6M LiI 0.3 M I₂	35		1.61	113	0.31	0.057
[21]	NiO/graphene	30	400	N719	0.8 M LiI and 0.15 M I2 in acetonitrile	1	7	0.27	105	33	0.0094

EC, ethylene carbonate; PC, propylene carbonate; DMII, 1,3-dimethylimidazolium iodide; DMPII, 1-propyl-2,3-dimethylimidazolium iodide; MPN, methoxypropionitrile; TBP, 4-tertiary butylpyridine; GuaSCN, guanidinium thiocyanate; VN, valeronitrile; ERY, erythrosine B. (A) Glass substrate was kept at room temperature during the spraying of NiO nanoparticles. (B) Substrate heating 60–708 C while the NiO slurry was sprayed onto the glass (NiO 2 samples). (C) Plasma bombardment of the bare substrate (NiO 3 samples). Substrate heating 60–708 C while the NiO slurry was sprayed onto the glass (NiO 2 samples).

Flynn et al. [25] have since reported a detailed study on the effects of sintering temperature (100–600 °C) on the morphology of NiO electrodes prepared from Ni(OH)₂ nanoplatelets, which they prepared by adding NH₄OH to a refluxing aqueous solution of Ni(NO₃)₂. Conversion of Ni(OH)₂ to NiO was observed by powder XRD at 250 °C and increasing the annealing temperature increased the crystallite size from 9 to 15 nm at 250–400 °C to 18–25 nm at 500–600 °C. This was accompanied by a colour change from bright green for Ni(OH)₂ to black and then light grey. A decrease in surface area as the sintering temperature was raised from 350 to 450 °C was correlated with a 4-fold decrease in dye loading. At 550 °C and above the mechanical stability of the NiO films decreased and annealing above 600 °C led to the loss of all pore structure. The highest performance (J_{SC} and efficiency) was observed for samples calcined at 400 and 450 °C. The V_{OC} increased linearly with calcination temperature, reaching a maximum of 108 ± 4 mV at 500 °C. For the electrodes sintered at the optimum temperature for p-DSC efficiency (Table 1), 450 °C, a conductivity of $2.2 \pm 0.8 \times 10^{-3}$ S cm⁻¹, a doping density up to 7×10^{20} cm⁻³ and a mobility value of ca. 2×10^{-5} cm² V⁻¹ s⁻¹ (for commercial nanoparticles treated under the same conditions they obtained: $6 \pm 1 \times 10^{-5}$ S cm⁻¹; 3×10^{20} cm⁻³; 1×10^{-6} cm² V⁻¹ s⁻¹). The effective mobility decreased dramatically from 350 to 550 °C which was attributed to changes in the stoichiometry or chemistry of the NiO surface as evidenced by XPS which showed progressively decreasing signals from hydroxylated/defective NiO with increasing annealing temperature. They also reported a 30% higher efficiency for their nanoplatelet devices compared to devices fabricated with commercial nanoparticles under the same conditions and annealed at 450 °C.

A real breakthrough came in 2008 when Qin et al. [26] developed the "push-pull" dye, P1 (Fig. 3), specifically designed for photocathode devices. p-DSCs prepared from Ni(OH)₂ calcined at 300 °C for 30 min produced a J_{SC} of 1.52 mA cm⁻² with an IPCE of 18%. Doubling the film thickness by annealing a layer of Ni(OH)₂ and then depositing and annealing a second layer and switching the electrolyte solvent from propylene carbonate to acetonitrile lead to an increase in J_{SC} to 2.5 mA cm⁻² and IPCE to 35% [27].

Le Pleux et al. [28] succeeded in increasing the NiO film thickness further by depositing NiO using a solvothermal route (Fig. 5). Porous and nanostructured thin films of NiO 3.5 μm thick were prepared on FTO coated glass by annealing films obtained from nickel acetate in the presence of hexamethylenetetramine under hydrothermal conditions (100 °C in a sealed autoclave). p-DSCs using coumarin C343 as sensitizer gave higher values of V_{OC} (117 mV compared to 80 mV reported by Zhu [24] and 70 mV reported by Qin [26]) and J_{SC} (0.88 mA cm⁻² compared to 0.35 mA cm⁻² reported by Zhu and 0.78 mA cm⁻² reported by Qin). The authors also reported better reproducibility for p-DSCs prepared using this route compared to the doctor blade technique with the advantage that relatively thick, crack-free films with good adhesion to the FTO surface could be prepared in fewer steps.

Evidence from thermal analysis of the green films deposited on the conductive glass in the autoclave suggests that annealing the film at 350 °C in air converts Ni(OCOCH₃)₂·2H₂O to NiO via Ni(OH)₂. The average crystallite size estimated from the X-ray diffraction pattern was 11 nm. SEM images of the NiO (Fig. 6) reveal their spongy nature with ca. 10 nm thick "nanoleaves". The film thicknesses varied linearly with the reaction time until 350 min (4.4 μm thickness). The specific surface area of the 3.5 μm thick NiO film, determined by the Brunauer–Emmett–Teller (BET) and the Barrett–Joyner–Halenda (BJH) methods was estimated to be 61 m² g⁻¹, a value which compares well with some TiO₂ films used for n-DSC [29], and the porosity reveals a narrow Gaussian pore size distribution centred at 8 nm with a full width at half-maximum of about
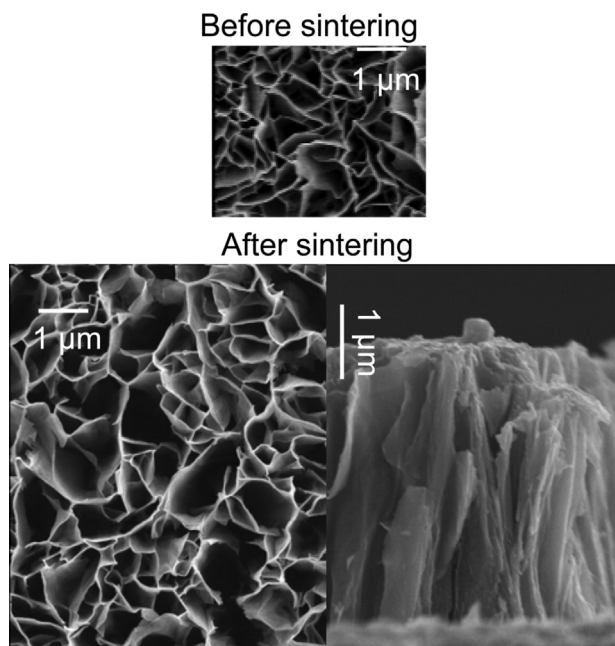
Before sintering

After sintering

Fig. 5. SEM images of the Ni(OCOCH$_3$)$_2$.4H$_2$O film before and after annealing. Reprinted with permission from Ref. [28]. Copyright 2009 American Chemical Society.

6 nm. This dense, open structure with a high surface area for dye adsorption was beneficial for generating high photocurrents.

Wang et al. [30] improved the hydrothermal route by sequentially depositing layers of NiO, doubling the efficiency compared to a single hydrothermal treatment. FTO coated glass substrates were treated in an autoclave containing a solution of NiCl$_2$·6H$_2$O and (CH$_2$)$_6$N$_4$ for 30 h at 90 °C and then calcined at 350 °C. In order to reduce the formation of large particles and to keep the surface of the film more uniform, the solution in the autoclave was replenished every 5 h. SEM images reveal 5 μm layers up to a thickness of 15 μm for the best DSCs (from a 25 mM precursor solution) but a maximum of 45 μm was reported when higher concentrations of precursor solution were used (75 mM). Analysis of the XRD patterns gave average crystallite sizes of approximately 2 nm. The concentration of the precursor solution affects the band gap of the material, decreasing in energy (from 4.73 eV to 3.98 eV) as the concentration of NiCl$_2$ was increased, indicating a quantum size effect. The

BET specific surface areas of the films where the solution was not replenished were similar to those reported by Le Pleux [28] whereas the surface area for the films where the solution was replenished was much higher (94.066 m^2 g^{-1} compared to 58.9 m^2 g^{-1}).

Qu et al. [31] modified the procedure by heating Ni(OAc)$_2$ at reflux (170 °C) in ethylene glycol, dispersing the green precipitate that formed in ethanol and water and heating the suspension at 150 °C for 12 h in an autoclave. The β-Ni(OH)$_2$ produced was applied to FTO glass by doctor blade and the electrode was annealed at 400 °C for 2 h to obtain NiO. The BET surface area (133 m^2 g^{-1}) was higher than that reported by Le Pleux [28] and Wang [30] above, as was the efficiency of the p-DSC (0.09%, Table 1) Qu et al. [31] also commented on the importance of the calcination temperature on the DSC efficiency. The authors stated that the surface area and pore volume decreased as the temperature increased but crystallinity increased with temperature and above 400 °C the stability of the film was poor.

Odobel et al. [32] reported the presence of Ni^0 in films prepared using Le Pleux's [28] route and suggested that the annealing temperature chosen is not sufficiently high to fully oxidize Ni(OCOCH$_3$)$_2$·4H$_2$O in air. They commented that "most preparation routes of NiO films for DSCs applications reported in the literature are based on similar thermal treatments in air. In that respect, we may infer that all these preparation routes systematically lead to the presence of Ni^0 metal and explain the black colour found in thick photocathodes." Flynn et al. [25] have responded that they found no evidence for Ni^0 in their NiO material or electrodes. Likewise, the powder XRD patterns reported by Qu et al. [31] and Wang et al. [30] do not contain appear to contain peaks corresponding to Ni^0. The text-book explanation of the colour in NiO is that Ni^{2+} vacancies lead to the formation of Ni^{3+} impurities which are responsible for the p-type conduction character and the colour, due to the corresponding charge transfer transitions [33–36]. Indeed, NiO is a well-known electrochromic material, undergoing a colour change from green to black when a positive potential is applied, and the spectroelectrochemistry has been reported in detail by Boschloo et al. [37] Doping with Li$^+$ to form Li$_x$Ni$_{1-x}$O is known to increase the conductivity and the black colouration [36,38].

Another successful method to prepare mesoporous NiO electrodes is to use templates based on polyethyleneoxide–polypropyleneoxide–polyethyleneoxide. Triblock copolymers have been extensively applied to sol–gel preparation of various metal oxides for a range of applications [39,40]. Films prepared in this way have characteristically uniform particle and void sizes suggestive of a long ordered Ni-polymer meso-structure before
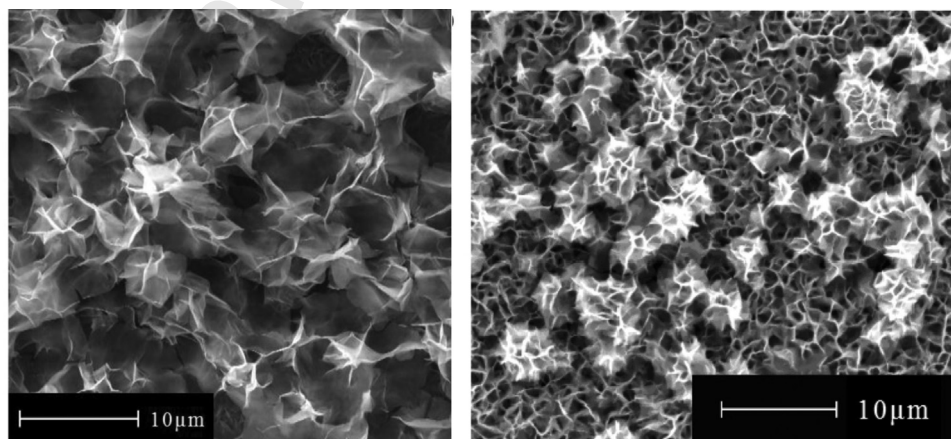

Fig. 6. SEM images of NiO prepared solvothermally from a 25 mM precursor solution. Left = 30 h deposition time, Right = improved method replenishing the solvent every 5 h. Reprinted from Ref. [30]. Copyright 2013, with permission from Elsevier.
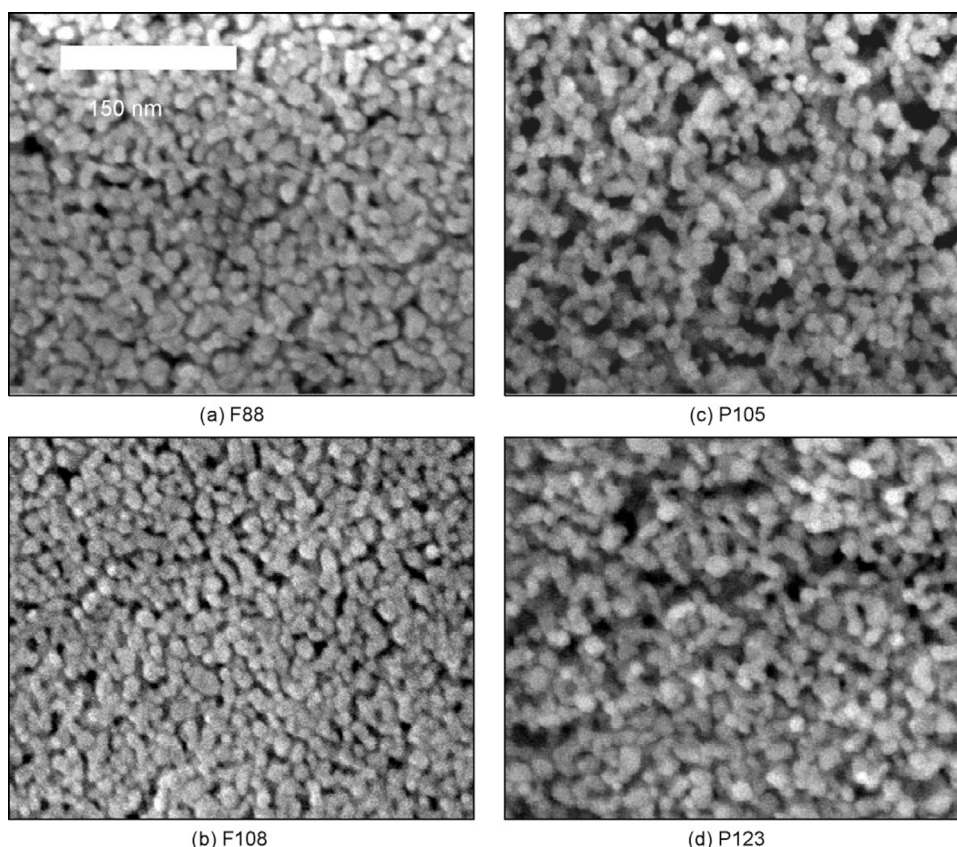
Fig. 7. Field emission SEM images of nanoporous NiO films synthesized using F group polymers (a and b) and P group polymers (c and d). Reprinted from Ref. [41]. Copyright 2008, with permission from Elsevier.

calcination. Nakasa et al. [4] were the first to apply this method to prepare NiO cathodes for p-DSCs. The authors deposited a precursor solution containing a triblock copolymer template $(HO(OCH_2CH_2)_{20}(OCH(CH_3)CH_2)_{70}(OCH_2CH_2)_{20}OHCH_2,$ P123) and $NiCl_2$ in ethanol and water onto FTO conductive glass by spin-coating. The material was calcined at 450 °C to give crack-free, 1 μm thick, nanostructured (30–40 nm), NiO films. p-DSCs using a merocyanine dye (3-carboxymethyl-5-[2-(3-octadecyl-2-benzothiazolinyldene) ethylidene]-2-thioxo-4-thiazolidine, NK-2684) (Fig. 3) as the sensitizer gave $J_{SC} = 1$ mA cm^{-2} and $V_{OC} = 93$ mV. Sumikura et al. [41] compared NiO p-DSCs prepared using different templates based on triblock copolymers with different polyethylene oxide (PEO)/polypropylene oxide (PPO) ratios. The sol gel precursor was deposited on an FTO glass substrate by the doctor blade method, dried at room temperature and then calcined in air. The calcination temperatures required for the polymer template route are higher (400–450 °C) compared to the template-free routes described above (300–350 °C) in order to burn off the organic components. Solar cells prepared with a higher PEO/PPO ratio gave a three-fold higher photocurrent compared to those prepared with polymers with a lower PEO/PPO ratio. This was attributed to a higher PEO/PPO ratio producing NiO with a larger surface area and smaller interparticle voids which resulted in two-fold higher dye-sensitization (Fig. 7 shows the SEM images). This is because hydrophobic PPO cores which form in the water/ethanol solvent become large voids after calcination, whereas the hydrophilic PEO segments tend to disperse uniformly forming small PPO cores and smaller voids. The Ni^{2+} ions residing in the hydrophilic environment (solvent and PEO) become particles after solvent vaporization and NiO crystals upon calcination. The crystalline size estimated from the powder XRD patterns ranged from 12.0 to 23.0 nm, and were consistent with the 10–20 nm size particles in the SEM images (Fig. 7). Therefore, unlike the template-free films above, the particles are not crystalline aggregates in the templated films, but individual crystals. The particle size can also be tuned with the Ni/polymer ratio, e.g. a lower ratio of $NiCl_2$/PEO gives smaller crystals (Table 2).

In 2010, Li et al. reported another breakthrough in the performance of p-DSCs when they combined the P1 dye with NiO prepared by the F108-templated method described by Sumikura et

Table 2

Molecular constitution of the PEOmPPOnPEOm polymers used by Sumikura et al. [41][a].

Polymer	MW	m/n	Particle size (nm)	BET Surface Area (m^2 g^{-1})	Dye adsorption (μmol cm^{-3})	IPCE (%)
F88	11,400	2.67	18.6	41.7	450	16
F88L			23	32.4		7
F88S			15.3	61		7
F108	14,600	2.66	12	43.6		17
P105	6500	0.66	19	39	240	8
P123	5750	0.29	20.4	22.8		7

[a] The polymers having longer PEO chains are classified in F group, and those having shorter PEO chains are in P group. L and S refer to the NiCl$_2$/polymer ratio: L = 3.3; S = 0.3; all others = 1 by weight. Particle size was calculated by the Sherrer formula using XRD data and BET surface area. IPCE is taken at 500 nm.
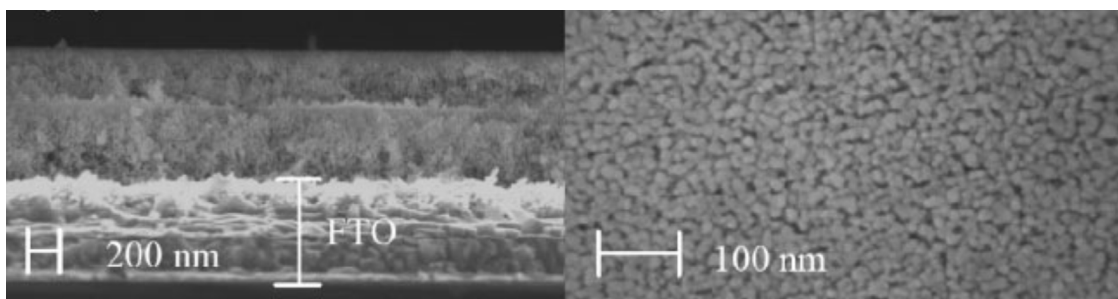
Fig. 8. SEM image of (a) a cross-section and (b) surface of NiO films prepared in two steps.
Reproduced with permission from Ref. [9]. Copyright 2010, with permission from Wiley.

al. [41]. The IPCE increased from the previous 35% for P1-sensitized NiO prepared by the dehydration of Ni(OH)$_2$, to 64% for the polymer templated NiO. Thicker films 1.1–1.2 μm compared to 0.5 μm reported by Sumikura et al. [41] were made by doctor-blading a precursor solution onto conducting glass substrates in two steps and sintering in between applications. Fig. 8 shows the SEM images which suggest a dense, highly ordered film of NiO nanoparticles. The crystal sizes of the NiO were calculated to be 16 nm in both films from the broadening of the X-ray diffraction peaks, three times larger than the NiO used in the previous studies described above. Brautigam et al. have reported a novel synthetic route to NiO nanostructures using various amphiphilic polystyrene-block-poly(2-vinylpyridine) (PS-b-P2VP) diblock copolymers as templates. The synthetic process contains several steps: including the dissolution of the diblock copolymer, addition of Ni^{2+}, followed by the formation of core–corona micelles and a further addition of Ni^{2+}, resulted in the formation of a macroscopic precipitate. This precipitate was deposited on solid substrates and calcination resulted in the formation of NiO films. A variety of different morphologies was found, including spherical particles, toroid structures and networks. The BET value obtained of about 50 m^2 g^{-1} is comparable to the value for conventionally obtained NiO surfaces. The NiO surface fabricated in this manner was successfully sensitized with the coumarin 343 dye [42,43].

The most straightforward route to reproducible NiO electrodes is to use pre-formed NiO nanoparticles. Awais et al. [44] deposited a suspension of 40 nm NiO nanoparticles in 2-propanol on to ITO-coated glass by spraying. Different thicknesses (0.3–3 μm) were prepared by tuning the spraying time: a single pass gave a thickness 0.4 μm, 3 passes gave a thickness of 1.5–2.0 μm and 5 passes gave a of thickness 2.5–3.0 μm. The films were then annealed in air to sinter the particles. Fig. 9 shows the SEM image of the surface of the film. For p-DSCs prepared with erythrosin B as a sensitizer, improved photocurrents and photovoltages were obtained compared to those reported by He et al. [1] using the Ni(OH)$_2$ sol–gel preparation method and Nattestad et al. [45] (below) using a paste prepared with commercial NiO nanoparticles (see Table 1). The benefit of the spray deposition route is that, unlike screen-printing and sol–gel based methods, the alcohol suspensions of NiO nanoparticles do not contain organic additives that require combustion during the annealing process and add to the preparation costs. Heating the substrate to 60–70 °C during the spray deposition improves the performance compared to keeping the substrate at room temperature.

When P1 was used as the sensitizer, a conversion efficiency η = 0.12% and incident photon-to-current conversion efficiencies IPCE = 50%, with relatively high photovoltages (up to 135 mV) for a p-DSC containing the triiodide–iodide redox couple, were obtained for NiO electrodes having a thickness of 1.5–2.0 μm.

Conventional sintering in a furnace was compared with a newly developed rapid discharge sintering (RDS) method for spray-deposited NiO (Fig. 10 shows the SEM images of the surfaces) [46,47]. RDS is based on microwave-assisted plasma formation and, as well as reducing the sintering time (5 min) substantially, it differs from a conventional furnace by transmitting heat from the bulk of the sample outwards, with controlled confinement of the heating zone. p-DSCs with P1 as the sensitizer gave comparable results and when erythrosine B was used the performance was better for the samples annealed using RDS (Table 1).

The most common technique used for the preparation of n-DSCs is to deposit a paste of pre-formed TiO$_2$ nanoparticles with an organic binder onto the conductive glass by spreading with a glass rod (doctor blade) or screen printing [48]. Nattestad et al. [45] developed this route, preparing a slurry of 20 nm NiO particles in acetylacetone, triton X 100, and distilled water and applying it to FTO coated glass by the doctor blade technique. A centrifugation step was necessary to remove larger agglomerates from the slurry and achieve smooth crack-free films of up to 1.6 ± 0.1 μm thickness. A range of dyes were compared by Nattestad et al. [45] and the highest conversion efficiencies were obtained for coumarin 343, followed by erythrosin J (Table 1.) Erythrosin J gave the highest open-circuit potential, 122 mV. Subsequently, the authors developed a screen printing paste, similar to that used for TiO$_2$ n-DSCs [2,49] by mixing a slurry of NiO nanoparticles in ethanol with ethanolic ethyl cellulose and terpineol, followed by slow ethanol removal by rotary evaporation. Sensitizing their 2.3 μm thick NiO electrodes with the PMI6-TTPA dye developed
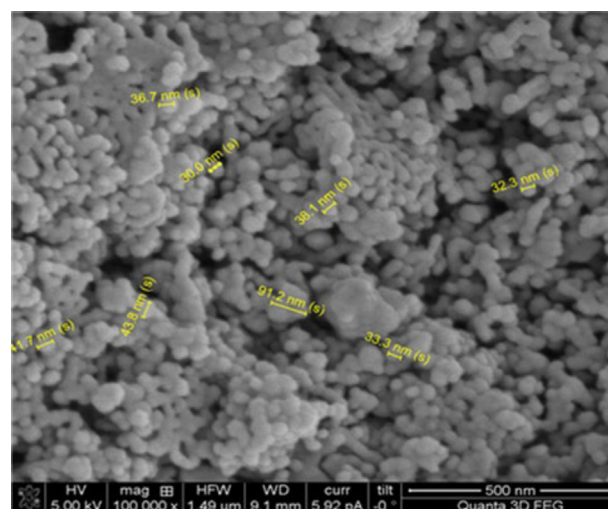

Fig. 9. SEM image showing the surface morphology of a NiO layer (*l* = 2–3 μm) deposited onto Sn:In$_2$O$_3$ (ITO) via spray deposition followed by annealing. The particle diameter is distributed between 30 and 90 nm (shown in yellow).
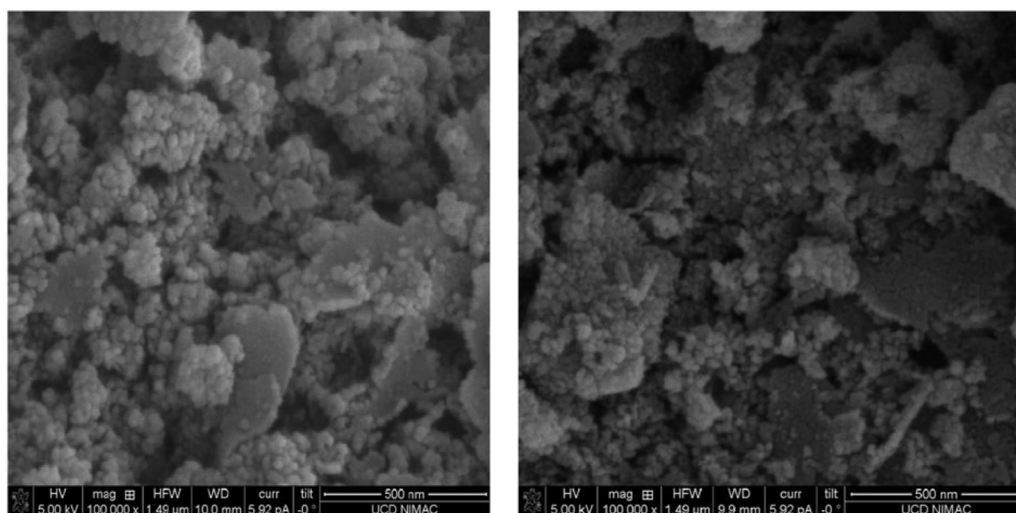Reproduced from Ref. [44] with kind permission from Springer Science and Business Media.

Fig. 10. SEM images showing the surface morphology of (left) sample sintered in a furnace and (right) sample sintered using rapid discharge sintering (RDS).
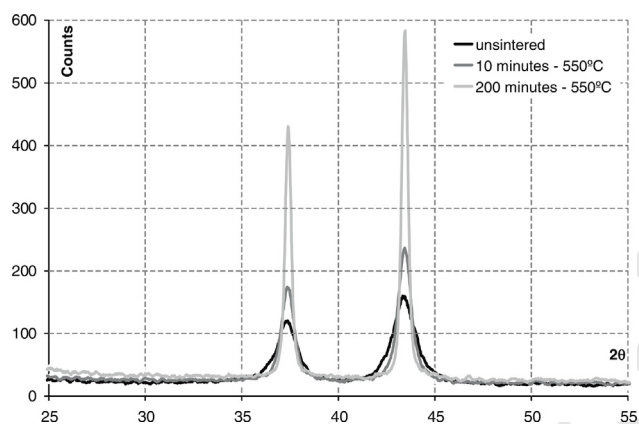Reproduced from Ref. [46] by permission of the PCCP Owner Societies.

Fig. 11. XRD pattern for NiO films sintered for different times showing sharpening of the peaks at 37.25° (1 1 1) and 43.28° (2 0 0). The XRD results also show the absence of Ni metal (45.502° and 53.045°).
Reproduced with permission from Ref. [45].

by the Bäuerle group [50] (see Fig. 3) and assembling them in p-DSCs generated an impressive IPCE of 62% and device efficiency of 0.41%. A photocurrent density of 7.57 mA cm^{-2} (0.35% efficiency) was obtained by modifying the dye with oligo-fluorene linkers rather than oligo-thiophene [49]. However, a record conversion efficiency of 0.61% for a p-DSC containing the I_3^-/I^- electrolyte was achieved by improving the nanoscale crystallinity of NiO [51]. A significant enhancement of photovoltage and fill factor was achieved by dip coating the substrates in nickel acetate and drying them prior to screen printing and annealing in air at 450 °C and applying an additional post-treatment at 550 °C for 15 min.

Annealing the film at the optimal temperature, 550 °C, increases the crystal size and eradicates smaller crystals and amorphous material as the decrease in surface energy drives diffusion and grain growth (Figs. 11 and 12 show the peak sharpening in the XRD pattern and TEM images suggesting the improved crystallinity by the post-treatment at 550 °C). This reduces the photovoltaic active internal surface area (see Table 3), and leads to reduced light harvesting efficiencies. However, the number of small pores which are poorly accessible to the electrolyte and would result in poor dye-regeneration and increased charge recombination are reduced. Sintering also establishes inter-particle necking, which is also
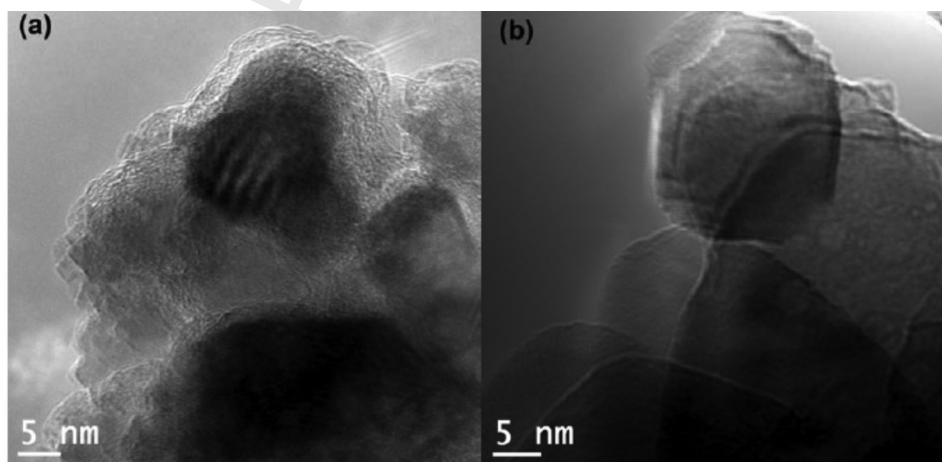

Fig. 12. HRTEM images of NiO nanoparticles (a) after sintering at 450 °C showing the presence of the amorphous shell around the nanoparticles, (b) after the post-treatment at 550 °C showing clear lattice fringes at the edge of the nanoparticles suggesting improved crystallinity.
Reproduced from Ref. [51] with permission from The Royal Society of Chemistry.

Table 3
Surface area and porosity data determined from BET data and average crystallite size determined from powder XRD data for NiO sintered for various times.

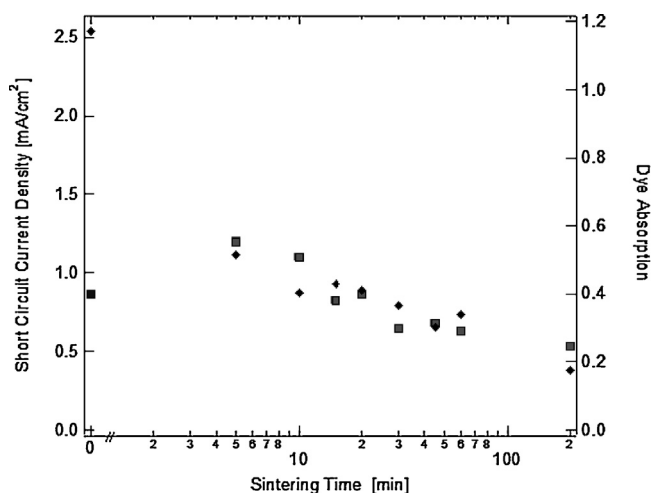| Reference	Sample	Surface area ($m^2\ g^{-1}$)	Porosity Major pore size (%)	Average crystallite size (nm)
[45]	Unsintered film	122	59	14
[45]	10 min at 550 °C	56	51.2	22
[45]	200 min at 550 °C	12	39.9	45
[51]	30 min at 450 °C	55	8.5 nm	
[51]	30 min at 450 °C +15 min 550 °C	34	15.3 nm	
[53]	nanorods 30 min at 450 °C+15 min 550 °C	29.7	20–40 nm	10×100 nm
[12]	microballs30 min at 450 °C+15 min 550 °C	65	68%	ca. 25 (3 μm)

Fig. 13. Plot showing that increasing the sintering duration causes an increased then decreasing normalized absorption (at 400 nm) of dyed films (diamonds) and the corresponding trend in J_{SC} (squares).
Reproduced with permission from Ref. [45].

known to strongly affect the charge collection efficiency in nano-structured TiO_2 films [52]. Therefore the photocurrent increases initially when the films are annealed compared to devices prepared from unsintered films, despite lower dye loading and light harvesting. The optimized annealing time was reported to be 5–20 min (see Fig. 13) [45].

Despite the largely reduced surface area of the mesoporous NiO film which underwent post-treatment at 550 °C only a negligible drop in photocurrent from 5.40 mA cm^{-2} to 5.11 mA cm^{-2}, was observed. This implies that any adverse effects due to the decrease in surface dye uptake were compensated by a better light harvesting and/or a more efficient charge collection process in the films with the post-treatment. The improvement in efficiency for the films given a 550 °C post-treatment compared to their previously published results (Table 1) is most likely a results of the relatively high photovoltage (V_{OC} = 294 mV). Table 3 summarizes the conditions and properties of the NiO reported by the Australian groups.

In addition to organic templates, inorganic structure-directing agents have also been used with success [53]. Zhang et al. prepared highly crystalline NiO nanorods with average diameters of <10 nm and an aspect ratio of approximately 10, using mesoporous SiO_2 as a template (Fig. 14). A nanorod structure is a desirable morphology because of their potential to improve charge transport along the long axis. The authors prepared the nanorods from a sol–gel containing Ni(NO$_3$)$_2$,6H$_2$O and tetraethyl orthosilicate and P123 in ethanol and HCl by calcining the dried gel at 500 °C for 6 h followed by removing the silica with 2 M NaOH. They then prepared a screen-printing paste with ethyl cellulose and terpinol to deposit the material onto FTO glass. Sequential printing and drying (125 °C) steps gave films 1.7 μm thick which were sintered in air as above (450 °C for 30 min then at 500 °C for 15 min) before sensitizing and assembling them in p-DSCs. Mesoporous NiO films
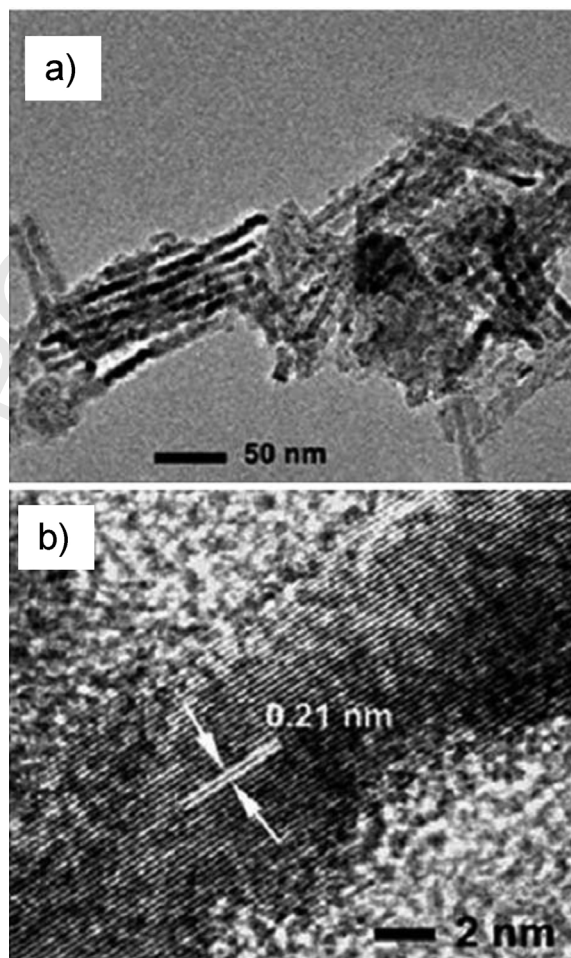

Fig. 14. TEM and High resolution TEM images of NiO nanorods reported by Zhang et al. The lattice fringes are clearly identified at the edge of the nanorod showing good crystallinity.
Reproduced from Ref. [53] with permission from The Royal Society of Chemistry.

utilizing these nanorods, compared to films prepared from commercial NiO nanoparticles, had similar surface area but narrower pore size distribution (see Table 3). When used as dye-sensitized photocathodes, NiO nanorod films had higher fill factor (ff = 0.42) and photovoltage (V_{OC} = 300 mV) and 30% higher overall efficiency (η = 0.4%) compared to a 1.7 μm thick electrode prepared from commercial nanoparticles.

0.46% efficiency was reported by Powar et al. [12] for a p-DSC based on nanostructured NiO microballs synthesized by thermolysis (Fig. 15). The authors heated an aqueous solution of Ni(NO$_3$)$_2$, oxalic acid dihydrate and hexamethylenetetramine for 5 h to give a green precipitate which was isolated and dried before it was calcined in air at 400 °C for 2 h, resulting in a fine grey powder. As for the nanorods above, a screen printing paste was prepared with ethyl cellulose and terpinol and the printed electrodes were
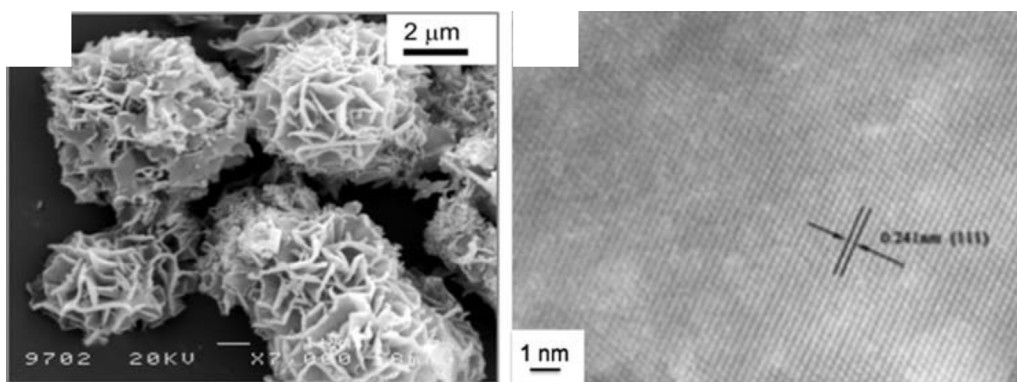
Fig. 15. SEM and (c) HRTEM images of as-synthesized NiO microballs.
Reproduced from Ref. [12] with permission from The Royal Society of Chemistry.
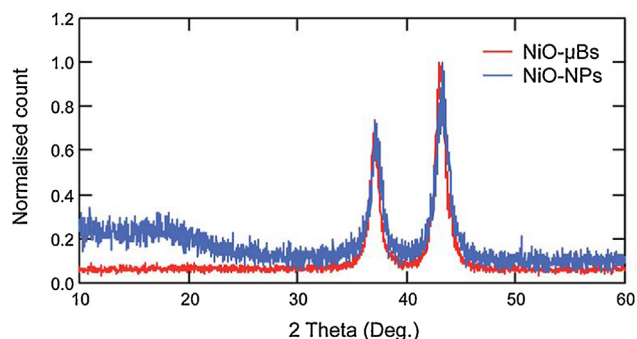

Fig. 16. XRD spectra of synthesized NiO microballs (red) and as-received NiO nanoparticles (blue).
Reproduced with permission from Ref. [12].

sintered at 400 °C for 30 min and 550 °C for 10 min. One screen printed layer gave an average thickness of 2.8 μm, corresponding to roughly a monolayer coverage of 3 μm microballs, two layers were 4.2 μm and three layers were 6.0 μm, subsequent print layers gave more uniform films. Despite consisting of similar crystal domain sizes compared to commercial NiO (Fig. 16), the dye uptake and light harvesting efficiency was higher for the NiO microballs. The amount of light absorbed parasitically by the NiO itself was lower for the NiO microballs (NiO nanoparticle-based DSCs absorbed ca. 31% of the incident photons, NiO-mBs based DSC absorbed ca. 24%), which the authors suggest could be due to a lower degree of defects in the NiO microball material. Both features led to the highest photocurrent observed so far for a p-DSC of 7 mA cm^{-2}.

3. Miscellaneous preparation methods

Apart from the NiO preparation methods outlined above several other approaches have been reported including methods based on electrochemical deposition [54–58], pulsed-laser deposition [59–61], plasma-enhanced chemical vapour deposition [62] and chemical bath deposition [63–65]. To the best of our knowledge they have not been used for the preparation of NiO surfaces for application in DSC devices. These methods are briefly discussed below.

Wu et al. [54] have fabricated NiO films for high capacitance supercapacitors. NiO is a promising metal oxide for alkaline supercapacitors due to its unique physical and chemical properties in alkaline electrolyte. The films are fabricated by anodic electrodeposition at a potential of +0.9 V (vs. Ag/AgCl) in the presence of a surfactant and the resulting films show high capacitance at slow scan rates (1110 F g^{-1} at 10 mV s^{-1}). Also, Djurišić

et al. [57] recorded a pseudo supercapacitance of 148 F g^{-1} at 100 mV s^{-1} from NiO layers fabricated by electrodeposition followed by annealing at 300 °C. NiO films have been reported for use in lithium-ion batteries where the formation of the films occurs via electrodeposition on copper plates and foam Ni substrates with subsequent heat treatment [56]. Enhanced electrochemical performance was reported for three-dimension porous morphologies of the foam NiO films and this method opens up a route to large scale fabrication of lithium-ion batteries with high-energy-density electrodes.

The magnetic behaviour of NiO films formed by pulsed-laser deposition (PLD) was studied by Katiyar et al. [61]. With this technique, NiO thin films were deposited in a DPL instrument from NiO pellets using a KrF excimer laser having emission at 248 nm. A polycrystalline film results and the size of the individual crystallites in the film can vary depending on the deposition conditions; films with smaller crystallite size exhibit superparamagnetic behaviour with antiferromagnetic behaviour displayed from films with larger crystallite size in the NiO layer. Such films are very attractive in applications such as spin valve sensors.

Plasma enhanced chemical vapour deposition has proved to be a successful technique for the controlled growth of NiO layers using either soda-lime glass, Si (1 1 1), stainless steel or fused silica as the substrates. Using metal acetylacetonato complexes as the source material, NiO and other metal oxide layers were formed at temperatures above 150 °C with each film having a smooth surface and columnar structure with growth perpendicular to the surface of the substrate [62].

Highly porous NiO films fabricated using chemical bath deposition (CBD) techniques have been reported for use as electrochromic materials [63]. The attractive properties of NiO such as high colouration efficiency, large dynamic range, low material cost and good cyclic reversibility have led to the use of this metal oxide in such an application [66]. Tu et al. [64] revealed that CBD NiO films exhibited superior behaviour in terms of electrochemical reversibility, higher reactivity and reaction kinetics compared to analogous films prepared with sol–gel methods. Zhang et al. [65] also reported the production of NiO films on ITO exhibiting attractive electrochromic properties such as an optical modulation of 83.7% at 550 nm with a response time of the electrochromic window of 1.76 s for colouration and 1.54 s for bleaching respectively. The films were prepared by immersion of the ITO substrate in a chemical solution containing nickel sulphate, for 10 min at 20 °C with vigorous stirring, followed by annealing at temperatures ranging between 300 and 500 °C in air for 1.5 h. These results by Zhang et al. [65] show that such NiO layers exhibit large optical modulation, fast switch speed and cycle durability therefore making them advantageous for practical applications in this area.
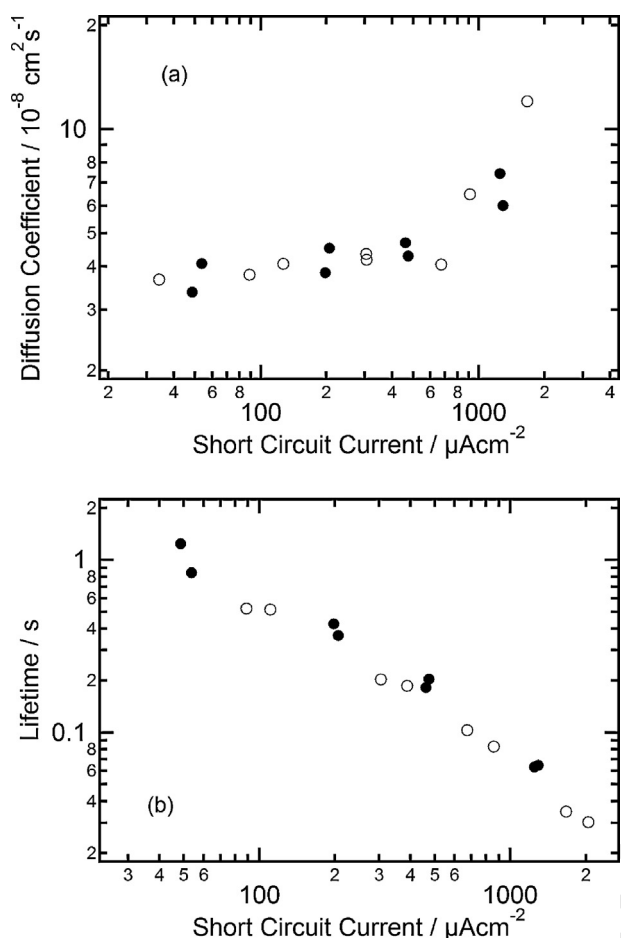
Fig. 18. Showing the dependence of τ_{tr} (open symbols) and τ_h (filled symbols) in C343-sensitized mesoporous NiO solar cells as a function of J_{SC} at the equivalent light intensity. The electrolyte was 0.5 M of LiI (circles), NaI (triangles) or Bu$_4$NI (squares) and 0.1 M I$_2$ in 3-methoxypropionitrile.
Reprinted with permission from Ref. [24]. Copyright 2007 American Chemical Society.

Fig. 17. (a) Hole diffusion coefficients (*D*) and (b) lifetime in fast-green sensitized NiO electrodes measured by small-amplitude light modulated photocurrent and photovoltage decay. Reprinted with permission from Ref. [10]. Copyright 2008 American Chemical Society. (b) Hole lifetime (τ_h) and hole transport time (τ_{tr}) (measured by EIS, IMVS, and IMPS) as a function of V_{OC}. Note that IMPS was carried out under short circuit, and the τ_{tr} here is plotted vs. the V_{OC} under the same light intensity. In each case the NiO was prepared using the F88 or F108 sol–gel route. Reprinted with permission from Ref. [68]. Copyright 2012 American Chemical Society.

4. Charge lifetimes and diffusion length in NiO p-DSCs

Several authors have reported optimum film thicknesses around 2 μm for NiO p-DSCs [12,24,46,51]. This is much thinner than the typical thickness of a TiO$_2$ electrode in a conventional n-DSC [67]. Typically, the photocurrent increase observed when the film thickness (path length) is increased is offset by a decrease in the open circuit photovoltage [44]. One reason is that for thicker films, the predominant contribution to the absorption of visible light comes from the NiO material itself. Increasing the film thickness from e.g. 2 to 3 μm may not improve the overall light harvesting efficiency sufficiently to counteract the increase in charge recombination when charges have further to diffuse before they are extracted at the FTO substrate. For example, Zhang et al. and Mori et al. have estimated hole diffusion lengths (*L*) of a few μm, which is only slightly higher than the NiO film thickness in their devices [10,51,53]. Zhang et al. measured a drop in the estimated charge collection efficiency from above 90% for light intensity lower than 0.1 sun to 80% at full sun, indicating that around 20% of the photogenerated holes are lost inside the device. This short *L* may explain the low fill factors (typically 0.3–0.4) for NiO p-DSCs. The large variation in *L* with light intensity means that a longer *L* does not always result in a higher IPCE [10] since the charge collection efficiency is nearly unity under the low light intensity used to measure IPCE, factors such as the
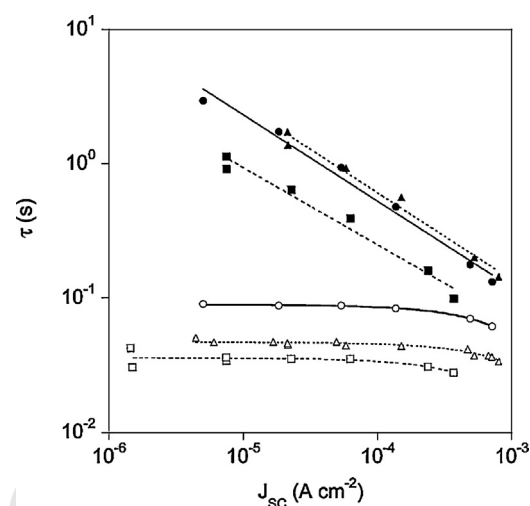
charge-separation efficiency limit the short-circuit photocurrent under these conditions and care must be taken in interpreting such data. To increase the efficiency of p-DSCs, *L*, which is much shorter than for electrons in n-DSCs [8,10] must be increased so that all the incoming light can be efficiently collected. This means that the time constants for hole transport must be decreased (τ_{tr}) and hole lifetime (τ_h) must be increased (Eq. (5)):

$$L = d\sqrt{(\tau_h/\tau_{tr})} \tag{5}$$

where *d*, the film thickness.

A number of authors have studied the charge lifetime and transport properties of NiO in p-DSCs [10,24,51,68] using small-modulation transient photocurrent and photovoltage measurements or electrochemical impedance (Fig. 17). The J_{SC} typically varies linearly with light intensity [24]. The time constant for hole transport and the apparent hole diffusion coefficients (*D*, Eq. (6)) varies little with bias light intensity for p-DSCs, and *D* only slightly increases as the concentration of holes in the NiO builds up at close to "1 sun". This is contrary to the transport of electrons in TiO$_2$ which is light intensity dependent as a result of trapping and de-trapping of electrons [69,70]. *D* is also typically much lower in magnitude than the typical values for electrons in dye-sensitized TiO$_2$ solar cells (4×10^{-8} cm^2 s^{-1}) [10,71], which is consistent with a different transport mechanism, such as hole hopping:

$$D = \frac{d^2}{2.77\tau_h} \tag{6}$$

Support for the "hole hopping" mechanism is provided by the dependence of τ_{tr} on the type of cation in the electrolyte solution, decreasing in the order Li$^+$ > Na$^+$ > Bu$_4$N$^+$ (Fig. 18) [24]. Zhu et al. attributed this to adsorption of the cations affecting the hopping of charge at the NiO/electrolyte interface, mediated by Ni^{3+} at the surface. Variations in the I$^-$/I$_3^-$ ratio do not appear to change *D* or τ_h.

Further evidence to support the "hole-hopping" transport mechanism, rather than trapping/detrapping of charges between the narrow valence band and the surface states has been provided by Wu et al. [72] who doped NiO with different quantities of CoO and assembled the materials in p-DSCs. CoO was chosen due to similar ionic radii and lattice parameters (both CoO and NiO have the rock salt structure). The F108-templated sol gel method described
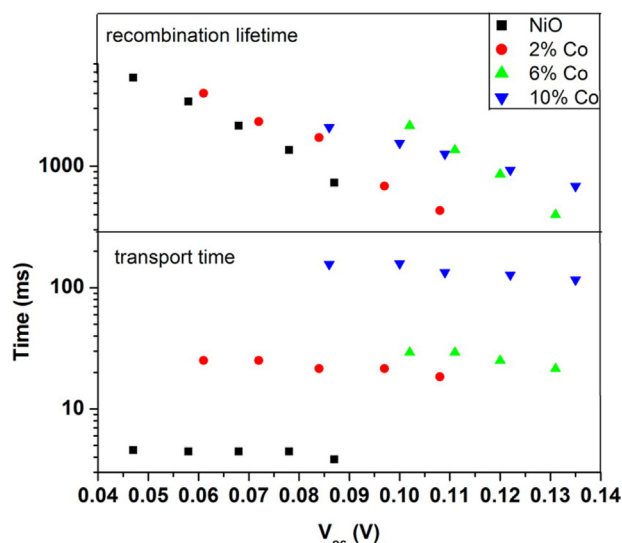
Fig. 19. Hole transport times within the pure and Co-doped NiO based p-DSCs plotted against short circuit photocurrents of the cells on a log–log scale. Carrier lifetimes (τ_h) for the pure and Co-doped NiO-based p-DSCs plotted against open circuit photovoltages of the respective cells on a semilog scale.
Reprinted with permission from Ref. [73]. Copyright 2012 American Chemical Society.

Fig. 20. Schematic representation of the recombination reaction between the redox mediator and the holes in the NiO valence band.

by Sumikura et al. [41] was used and to obtain the precursors for the doped samples, stoichiometric amounts (2, 6, and 10 mol % Co:Ni ratio) of anhydrous $CoCl_2$ were added to the initial solutions. Films of the solutions deposited in FTO glass by doctor blade annealed at 450 °C in air. The τ_{tr} increased from ∼5 ms for p-DSCs assembled with pure NiO cell by more than 2-fold for 2% and 6% Co-doped NiO films. Wu et al. [72] attributed this to the dopant ions acting as scattering centres for the electrons or holes, reducing the probability of polaron hopping and reducing the hole and electron mobility values. The transport times of the 10% Co-doped samples increased by an order of magnitude, indicating a very large density of defects. Consistent with the increase in charge transport time, the J_{SC} of the cells decreased slightly with Co doping at 2 and 6% compared to pure NiO and substantially upon 10% doping of cobalt. Since the transport depends on the mobility of the charge carriers and not on the carrier concentration, the small polaron hopping mechanism is more likely than band-like carrier transport.

The V_{OC} of the p-DSCs from 122 mV up to a maximum of 158 mV with >6% doping. This was consistent with the lowering of the flat-band potential (observed from Mott–Schottky measurements) of the NiO by a few tens of mV; higher hole lifetimes for the Co-doped cells than those for pure NiO cells and decrease in the dark current ("leakage current") of the devices with a higher percent of Co added. These observations point to an increased resistance to carrier recombination upon cobalt doping (Fig. 19).

These observations could partly explain the extremely fast recombination between the dye radical anions and the holes in the NiO observed spectroscopically [73,74]. A more efficient hole transfer process was observed for NiO nanoparticles pre-annealed in air as compared to vacuum [75]. Analysis of the Ni 2p3/2 peak in the XPS spectrum indicated that relatively more Ni^{3+} is formed in NiO annealed in air than in vacuum (The integrated peak area ratios of Ni^{2+}/Ni^{3+} = 0.51 and 0.75, respectively) This is rationalized in terms of oxygen creating Ni^{2+} vacancies causing some of the surrounding Ni^{2+} to undergo oxidation to form Ni^{3+} in order to preserve charge neutrality. The doping of nickel oxide films with Ni^{3+} results in a reduction of bandgap energy and an upward shift of the semiconductor valence band. The faster hole transfer rate observed for NiO annealed in air may be due to an energetically more favourable hole
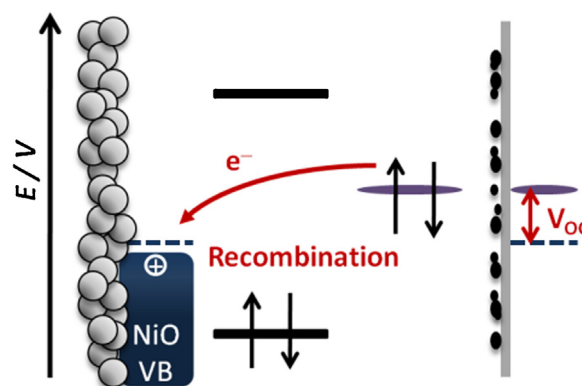
transfer process resulting from a larger energy difference between the HOMO of the dye and the valence band of NiO. Furthermore, the intraband gap states resulting from the formation of Ni^{3+} provide extra channels for charge transfer to take place, hence enhancing the hole transfer rates [10] resulting in larger D and similar τ and thus, longer L, for NiO electrodes prepared from commercial NiO nanoparticles compared to the F88 templated films. Li et al. [9] estimated the diffusion coefficient of F108-templated films (1.6×10^{-7} cm^2 s^{-1}) to be three times faster than in NiO electrodes prepared from Ni(OH)$_2$ colloids [26] (1.3×10^{-8} cm^2 s^{-1}), which partly explains the large improvement in J_{SC} and IPCE (see above). Zhang et al. [51] examined the effect of the post-treatment at 550 °C on D, measured from electrochemical impedance, and found little difference between post-treated and non-post treated electrodes (see above), suggesting that improving the crystallinity had little impact on the charge transport.

Hole lifetimes (ranging from 30 ms to 1 s) measured using these techniques are comparable in magnitude with electron lifetimes in dye-sensitized TiO$_2$ electrodes [10,24,71]. However, they decrease sharply (a power-law dependence) with increasing light intensity. Two factors could explain this: firstly, recombination between holes in the NiO and reduced species in the electrolyte is dependent on the concentration of holes in the NiO valence band and increasing the light intensity increases the rate of photoinjection; secondly, diffusion of triiodide in the pores is slow and, if the regeneration of the dye is kinetically limited, recombination between holes in the NiO and reduced dye molecules (Fig. 20) could increase with light intensity.

In general, τ_h is longer for electrodes made from pre-prepared nanoparticles compared to photocathodes prepared using sol–gel techniques where NiO is prepared in situ [46,51,53]. It is not clear whether this is because the crystal size is typically larger when pre-prepared NiO is used. The films prepared by spray deposition reported by Gibson et al. displayed some of the longest τ_h over the range 0.1–1 sun, in the order of 0.5–1 s. This is consistent with the reasonably high V_{OC} recorded with the P1 dye/triiodide iodide electrolyte. The decrease in τ_h vs. V_{OC} (light intensity) is less pronounced which indicates that charge recombination is supressed for the spray-deposited NiO in comparison to NiO electrodes with comparable thickness prepared using sol–gel techniques. Fig. 21 shows the trend in hole lifetime and diffusion time for pre-formed NiO nanoparticles with and without a second heating step at 550 °C. Zhang et al. measured τ_h >50% longer for NiO electrodes given the 550 °C post-treatment compared to films annealed at 450 °C only. This indicates that the improvement in V_{OC} brought about by sintering at 550 °C arises from a reduction in the rate of charge recombination at the NiO-electrolyte interface.
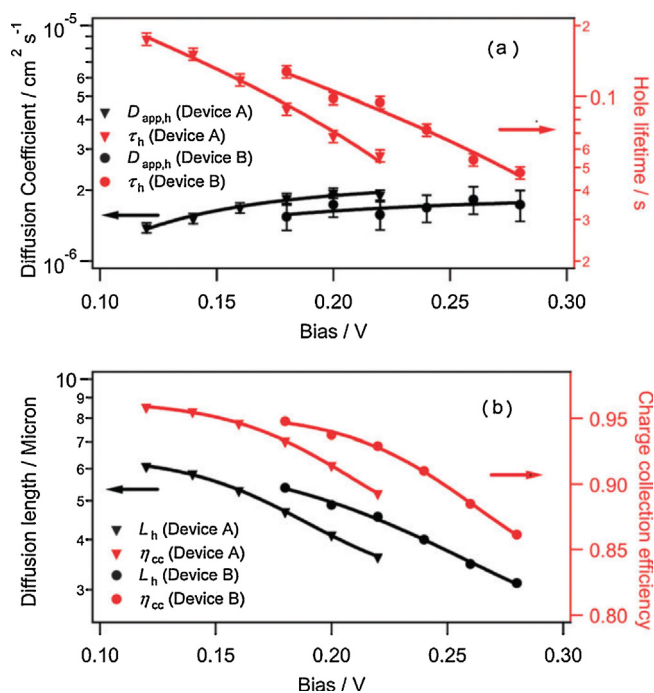
Fig. 21. (a) Apparent hole diffusion time (D) and hole lifetime (τ_h) for p-type DSCs made with NiO films without (Device A) and with (Device B) the post-treatment at 550 °C. The values were obtained by fitting electrochemical impedance (EIS) spectra of Devices A and B measured at different biases under the simulated 1 sun illumination. (b) Hole diffusion length (L_h) and hole collection efficiency (η_{cc}) of Devices A and B at the corresponding biases.
Reproduced from Ref. [51] with permission from The Royal Society of Chemistry.

In n-type DSCs the method of coating thin insulating layers of transparent metal oxides such as Al_2O_3 has been exploited in order to reduce the charge recombination to the electrolyte, particularly in the case of outer-sphere redox couples such as ferrocene and cobalt polypyridyl complexes [76–78]. Uehara et al. [79] coated porous NiO electrodes, prepared from commercial NiO, with Al_2O_3 by dipping them in an aluminium alkoxide solution in propanol at 60 °C for 20 min. On treatment, the peak maxima in the IPCE spectrum at 370 nm (due to the reaction with triiodide) decreased but increased at 520 nm (due to the reaction with the dye). The open circuit voltage, short circuit current density and energy conversion efficiency of the treated DSC were all higher than the non-treated DSC (Fig. 22). However, the τ_h decreased on treatment and decreased further when a higher concentration (30 mM) of the
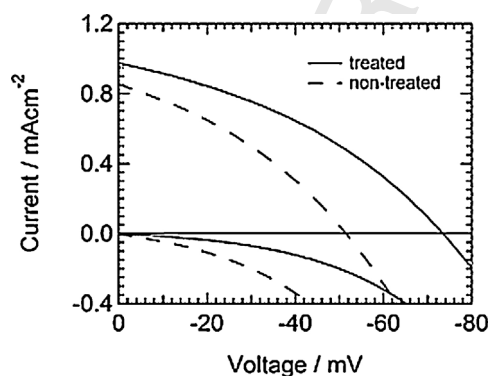

Fig. 22. Current–voltage curves of dye-sensitized Al_2O_3-treated NiO (solid line) and non-treated NiO (dashed line) solar cells under one sun and dark conditions. The thickness of both electrodes was ca. 1.4 μm. The concentration of Al(sec-butoxide)$_3$ solution was 2 mM. The temperature of treatment was 200 °C.
Reproduced from Ref. [79] with permission from The Royal Society of Chemistry.
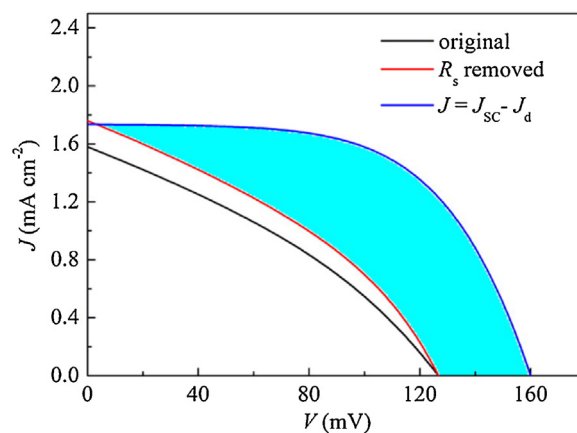

Fig. 23. Current–voltage curve after eliminating the effect of series resistance and recombination with reduced dye.
Reprinted with permission from Ref. [68]. Copyright 2012 American Chemical Society.

alkoxide solution was used. In other words, the recombination was enhanced by the insulating layer. A shift of the dark current curve to positive potential for the treated film compared to the untreated film, and an increase in V_{OC} for equivalent hole densities suggested that the valence band edge was shifted positively by modification of the film surface by a thin layer of aluminium oxide. The enhanced recombination could be a result of the increased potential difference (driving force) between the hole and I^-, and the decrease of surface trap density or the increase of surface I^- concentration.

Evidence from IPCE experiments and single molecule fluorescence showed that insulating Al_2O_3 layers can weaken the electronic interaction between the dye and NiO, on the one hand slowing the rate of charge separation at the dye-NiO interface, on the other slowing charge recombination and significantly enhancing photoelectric conversion efficiency [80].

One of the biggest factors limiting the efficiency of p-DSCs is low fill factor, which is a property of the resistive losses in the device [8]. As discussed above, holes localized at surface states may be mobile and, therefore, recombine easily with reduced dye molecules and electrolyte species. The lower dielectric constant of NiO means NiO is less effective in screening the Coulombic interaction between the charged dye and the charge carriers in the semiconductor than TiO_2 (NiO: ~11.9; TiO_2: 30–170; ZnO: ~8) [8,81–83]. Huang et al. [68] have examined the cause of the low fill factor in p-DSCs using EIS IMPS and IMVS. Fig. 23 shows a typical current–voltage curve in black. Removing the total series resistance (series resistance as measured by EIS + resistance of the counter electrode + transport resistance of the film) calculated from EIS gives the red line where the ff and η are enhanced by 6% and 19%, respectively. This shows that the transport resistance (and therefore D) has a small influence on the fill factor, possibly because the film thickness is small, even though D in p-DSCs is smaller than that in n-DSCs. The blue line in Fig. 23 is a plot of $J = J_{SC} - J_{dark}$. This has the expected diode shape of a current–voltage curve in accordance Eq. (7):

$$J_{net} = J_{photo} - J_0(e^{qV/mkT} - 1) \qquad (7)$$

where m is the diode ideality factor [13,47].

The ff and η are enhanced by 76 and 146%, respectively for the blue curve and the ff of the "corrected" cell is 0.60, which is approximately the theoretical value for the $V_{OC} = 160$ mV and $J_{SC} = 1.8$ mA cm^{-2} ($m = 0.93$). This shows there is a photo-process responsible for a large shunt resistance in p-DSCs. In addition, the current at reverse bias is frequently higher than at short-circuit (e.g. Fig. 22). Huang et al. ascribe the "photo-shunt" as being due to recombination between holes in the NiO with the reduced dye.

Several strategies described above have been applied to suppress the undesirable recombination reactions, in addition to synthesizing sensitizers with long-lived charge separated states such as PMI-NDI and PMI-6TTPA. Inspection of Table 1 does not reveal any support for any of these strategies addressing the "photo-shunt" as it includes dyes with different lifetimes, non-iodine-based electrolytes, different NiO crystal sizes and degree of crystallinity, yet all have fill factors roughly between 0.3 and 0.4. As a fill factor closer to 0.6 has not yet been achieved, the nature of this light-induced current-leakage process remains elusive.

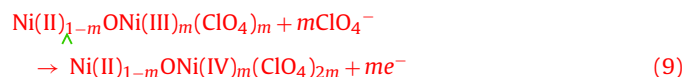## 5. Electrochemical properties of nickel oxide(s)

Because of the potential application of p-type nickel oxide in advanced solar conversion devices and optical technologies such as, electrochromic (EC) devices [84], energy storage systems [85], and dye-sensitized solar cells (DSCs) [1,12,41,86], a discussion of the electrochemical properties of the material is appropriate. In both EC and DSCs nickel oxide is applied as a thin film with thicknesses ranging from one hundred nm to a few microns [46,87]. Within this range nickel oxide is not totally insulating (vide infra), and shows an optical transparency with a transmittance of $T > 35\%$ in the visible range [88,13]. The utilization of thin electroactive films requires a supporting substrate which consists generally of few mm thick glass covered with a transparent conductive layer (TCL) of indium-doped tin oxide (ITO) or fluorine-doped tin oxide (FTO) [89] onto which nickel oxide is deposited. The presence of the TCL is necessary because of the high resistivity of undoped p-type nickel oxide ($\rho_{NiO} > 10^{10}\ \Omega\,cm$) [90] and the electrical contacts in nickel oxide based photo-electrochemical devices are made through the TCL, the electrical polarization of the oxide layer being achieved via the TCL/nickel oxide interface. The high electrical resistivity of pure nickel oxide also imposes the employment of films not thicker than 20 μm, besides the application of doping processes [91,92], in order to minimize the resistive effects of the oxide itself [93]. The thin film samples of the nickel oxide employed in EC devices and DSCs can present quite different morphologies (Fig. 24) [44,94–96], and consequently, different surface areas depending on the way the oxide is prepared and the processing temperature [9,12,53,94–97].

Among the methods of preparation of nickel oxide thin films the most important ones are sol–gel methods, based on the hydroxilation of nickel salts and successive annealing, sintering of pre-formed NiO nanoparticles with conventional furnace (CS) or plasma assisted microwave heating (RDS), magnetron sputtering in the reactive mode, microblast of preformed nickel oxide microparticles and spray pyrolysis. Besides morphology and surface area, the degree of crystallinity of the oxide can be also varied through the choice of opportune methods of preparation, the adoption of controlled deposition conditions and the modulation of the processing temperatures [44,94,95]. It has been generally observed that preparation methods have the most noticeable consequences on the extent of the current densities exchanged by the different oxide samples (kinetic effect), but have limited effect on the nature of the electrochemical processes [46,94,96]. This implies that the electrochemistry of nickel oxide can be systematically analyzed mostly in terms of the chemical composition of the resulting nickel oxide rather than in terms of the method of its preparation/deposition, which in turn will mostly affect the kinetic aspects of these electrochemical processes. Importantly nickel combines with oxygen to give several binary oxides that differ formally for the oxidation state of nickel [98]. The latter ranges between II and III with formation of the corresponding oxides NiO (green) and Ni_2O_3 (black) [99]. Within this class of compounds it is quite common to find also examples with non-stoichiometric features, which are generally described by the formula NiO_x and are characterized by the presence nickel atoms with different oxidation states including Ni(IV) [100]. In the analysis of these types of electrochemical processes one has to distinguish between: (a) nickel oxides representing the actual electroactive species undergoing oxidation/reduction processes [44,95,96]; (b) nickel oxides displaying electrocatalytic activity towards specific redox processes [101–103]. When the intrinsic electroactivity of unmodified nickel oxides is considered, the issues typical of solid state electrochemistry, e.g. ion intercalation/de-intercalation or charge-capacitance [104–106], have to be considered, whereas the analysis of the electrocatalytic activity of nickel oxides involves the analysis of the effect of the polarization on the electrical conductivity of the oxide [107], its band structure and density of states alteration [92,103,108] and how the frontier energy levels of the nickel oxides are positioned with respect to the redox level of the couple by varying the potential of the semiconducting electrodes [109,110]. In the particular case of the electrocatalytic effect of bare NiO towards triiodide reduction, i.e. the cathodic process of relevance in p-type DSCs [92,103], it has been recently found that mesoporous nickel oxide displays strong oxidative charge recombination [111] because of the matching between the upper edge of the NiO valence band and the I_3^-/I^- redox level [103], as well as the presence of bandgap states [92] the density of which increases towards energy values closed to the valence band upper edge. To decrease the extent of oxidative recombination some authors [103] have considered the modification of the NiO band structure by doping with lithium cations, which is equivalent to a process of p-doping. The most important consequence of Li^+ doping resulted in the lowering of the Fermi level of the doped vs. undoped oxide combined with the concomitant lowering of the trap states levels that are localized in the intragap. Moreover, the charge transfer resistance of the oxide towards iodide oxidation could be increased by doping NiO_x with Li^+ as observed with the increase of the potential threshold at which iodide is oxidized to triiodide [103,111].

Another factor that controls the electrochemistry of nickel oxides, either as electroactive species, or electrocatalytic materials, is the extent of hydration that transforms the nickel oxides into mixed oxy-hydroxides (partial hydration), or into hydroxides upon full hydration [100,112,113]. Hydration phenomena can occur if nickel oxide is stored either in an ambient environment, prepared from water containing precursors, or when immersed in an aqueous electrolyte [114,115]. The presence of hydrogen atoms in hydrated nickel oxides influences the electrochemistry of these oxides since hydrogen cations can be exchanged by the oxide to compensate for the variations in the oxidation state of the nickel centres (Eqs. (4) and (5)) (vide infra) [37,100]. In the following part the electrochemical properties of nickel oxide with nickel in the main redox state of 2+ will be reviewed considering oxidation in both anhydrous and aqueous electrolytes, and reduction processes in an anhydrous environment.

Both the reduction and the reversible oxidation of nickel oxide prepared via CS of pre-formed metal oxide nanoparticles could be observed in a single scan in water-free environment with anhydrous propylene carbonate as electrolytic solvent. The oxidation processes occurring at applied potential values larger than 2.5 V vs. Li^+/Li as a reference were ascribed to the nickel based redox reactions [44]:

$$NiO + mClO_4^- \rightarrow Ni(II)_{1-m}ONi(III)_m(ClO_4)_m + me^- \quad (8)$$

$$Ni(II)_{1-m}ONi(III)_m(ClO_4)_m + mClO_4^-$$
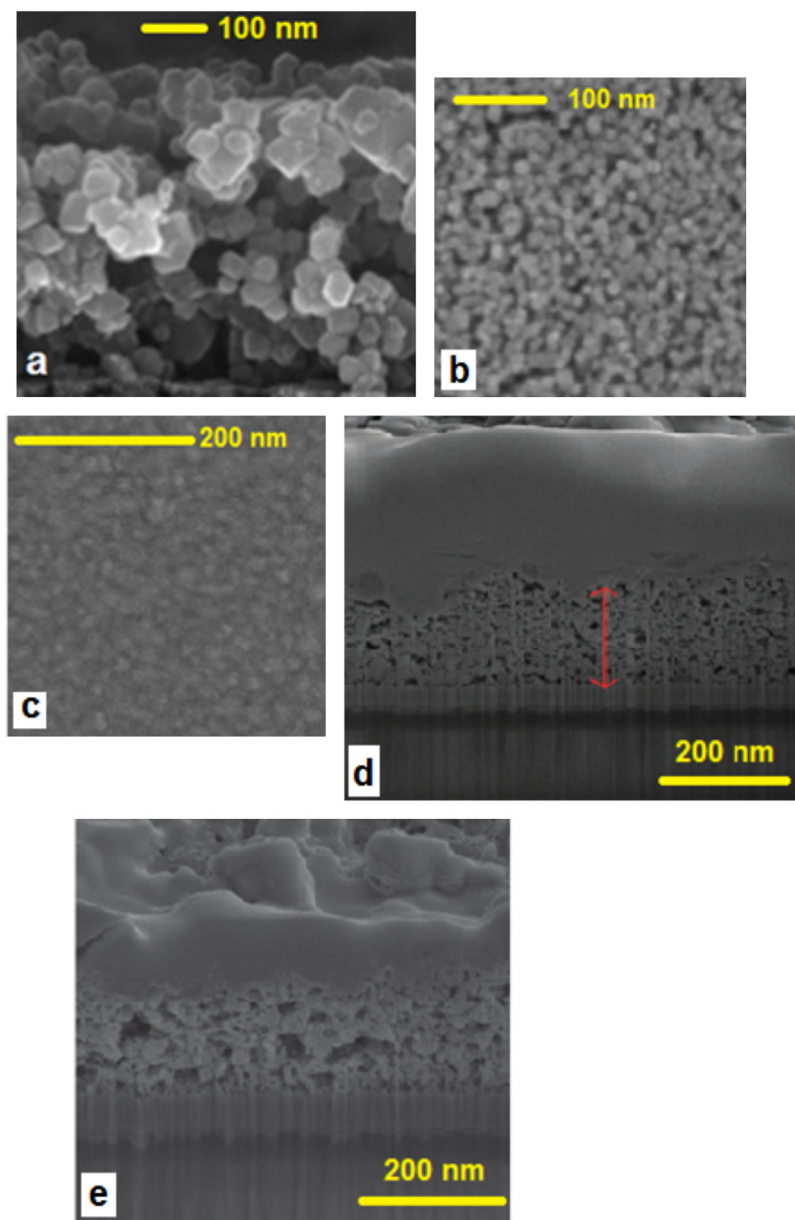$$\rightarrow Ni(II)_{1-m}ONi(IV)_m(ClO_4)_{2m} + me^- \quad (9)$$

Fig. 24. Morphologies of various nickel oxide thin films for DSC and EC applications, which have been obtained via diverse methods of deposition and under different processing conditions.
(a) Adapted from Ref. [98]; (b) adapted from Ref. [9]; (c) adapted from Ref. [97]; (d) and (e) adapted from Ref. [47].

The first broad an anodic peak centred at about 3.1 V vs. Li⁺/Li, and the second oxidation process with onset at about 3.4 V vs. Li⁺/Li. Eqs. (1) and (2) can both be regarded as processes of p-doping which are driven electrochemically. Participation of the ion perchlorate as charge compensating species in processes 1 and 2 was confirmed by the detection of chlorine atoms with XPS when differently polarized NiO samples were analyzed [100].

To further illustrate the electrochemical behaviour of NiO layers reported in our recent studies [44,46,47] some results will be discussed in more detail. Since oxidation of nickel oxide in anhydrous environment implies the uptake of relatively large anions localized either on the surface or within the structure of the metal oxide [116], electrochemical activation consisting in the continuous increase of the amount of current exchanged by a nickel oxide sample upon repeated cycling is generally observed (Fig. 25) [44].

This phenomenon is generally interpreted in terms of structure opening for nickel oxide as host material in order to favour the uptake of charged guests and minimize surface tension effects [117]. Since the reduction process of nickel oxide at potential values lower than 2.4 V vs. Li⁺/Li consists in the simultaneous uptake of electrons lodging in the electronic bands of NiO [92,103,118] and lithium cations in the oxide host according to [95,104,106]:

$$NiO + y Li^+ + y e^- \rightarrow Li_y NiO \qquad (10)$$

it is of no surprise that analogous phenomena of electrochemical activation are also observed when the reduction of nickel oxide is carried out (Fig. 26) [95,106].

Oxidation of nickel oxide is surface confined irrespective of the nature of the electrolyte, i.e. aqueous [38,46,86,100] or anhydrous [44], as determined by the linear dependence of the intensity of the current peaks with the scan rate [119]. In the case of the aqueous oxidation of nickel oxide, the potential values at which the two
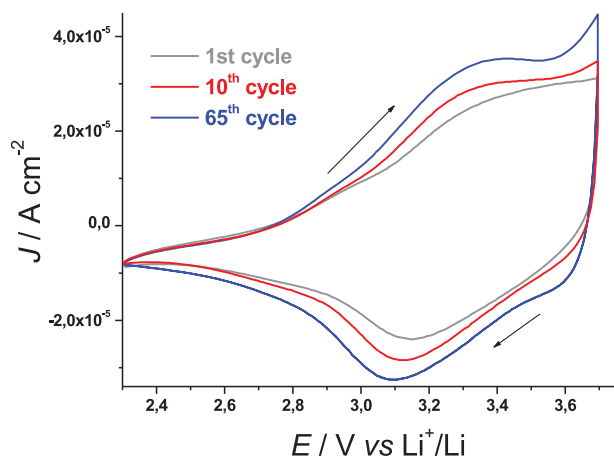
Fig. 25. Cyclic voltammetry of NiO prepared via rapid discharge sintering (RDS) of sprayed NiO nanoparticles with an average diameter of 50 nm. Substrate: ITO; electrolyte composition: 0.7 M LiClO$_4$ in anhydrous propylene carbonate; counter electrode: Li; reference electrode: Li$^+$/Li; scan rate: 5 mV s^{-1}. NiO thickness: 0.3 µm. The effect of the activation of NiO oxidation is shown with the increase of the current density upon continuous cycling.
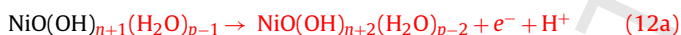Adapted from Ref. [45].

distinct processes occur are better resolved than in non-aqueous electrolyte (Figs. 27 and 28), and can be described as [44,100]:

$$NiO(OH)_n(H_2O)_p \rightarrow NiO(OH)_{n+1}(H_2O)_{p-1} + e^- + H^+ \tag{11a}$$

or

$$NiO(OH)_m \rightarrow NiOO(OH)_{m-1} + e^- + H^+ \tag{11b}$$

for the first anodic peak centred at about 0.5 V vs. Ag/AgCl with Eqs. (11a) and (11b) (as well Eqs. (12a) and (12b), vide infra) occurring to a different extent depending on the degree of hydration of the oxide. The second anodic peak centred at about 0.9 V vs. Ag/AgCl (Fig. 27), can be described as

$$NiO(OH)_{n+1}(H_2O)_{p-1} \rightarrow NiO(OH)_{n+2}(H_2O)_{p-2} + e^- + H^+ \tag{12a}$$

or

$$NiOO(OH)_{m-1} \rightarrow NiOO_2(OH)_{m-2} + e^- + H^+ \tag{12b}$$
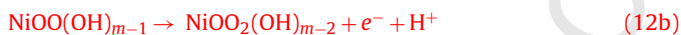
Unlike the behaviour observed in a non-aqueous environment, the electrochemical behaviour of NiO (either CS, RDS or sol–gel
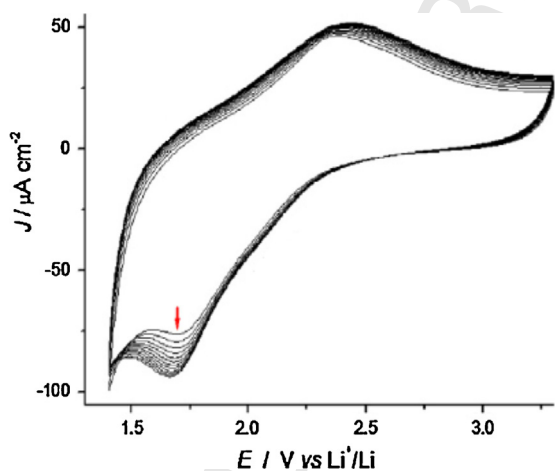

Fig. 26. Repeated cyclic voltammetry of microblast NiO deposited onto Ni sheet in the process of oxide reduction. Oxide film thickness: 1.2 µm; electrolyte composition: 0.5 M LiClO$_4$ in anhydrous propylene carbonate; scan rate: 40 mV s^{-1}. The red arrow indicates the evolution of the voltammogram upon repeated cycling.
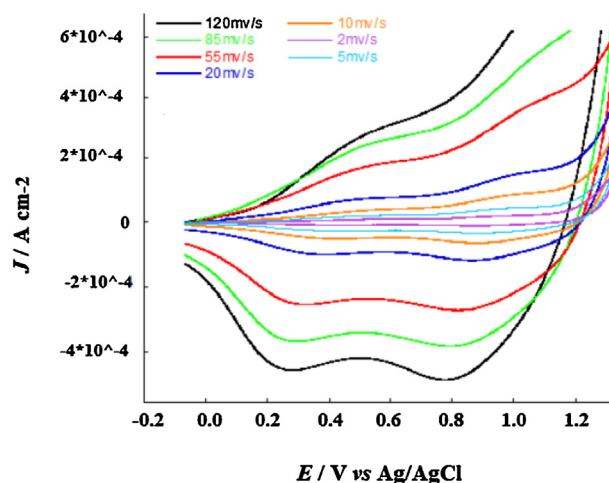Adapted from Ref. [97].

Fig. 27. Effect on the scan rate on the voltammogram of the NiO sample prepared via CS of 50 nm nanoparticles. Aqueous electrolyte composition: 0.2 M KCl, 0.01 M KH$_2$PO$_4$, 0.01 M Na$_2$HPO$_4$.
Adapted from Ref. [47].

prepared) in the presence of water is characterized by the progressive dissolution of nickel oxide upon repeated electrochemical cycling [100]. When NiO samples display a mesoporous morphology (Fig. 24(d) and (e)) the current exchanged by these type of samples is directly proportional to the thickness of the oxide coating [46]. Samples with a more porous morphology generate a larger oxidation current with respect to a less porous system with analogous thickness, mainly as a consequence of the larger surface area (Fig. 29) [46]. This feature is important if NiO is utilized as an electrode in DSCs or any other electrochemical device based on a redox process which is confined at the electrode surface. Among the two main scalable methods of NiO preparation, namely RDS and CS, RDS [46,96] procedures mesoporous NiO sample with larger surface area than CS, while allowing also for improved electrical connectivity within the NiO nanostructure.

The morphology of the matrix seems much less important for the reduction of NiO (Fig. 26 and Eq. (3)), than for NiO oxidation (Fig. 29) and the amount of current density exchanged by mesoporous NiO prepared via sol–gel, CS and RDS [95] and compact NiO prepared via sputtering or microblast [96] is quite similar irrespective of their substantially different morphologies (Fig. 24(c) and (d)). The occurrence of solid state oxidation/reduction in NiO
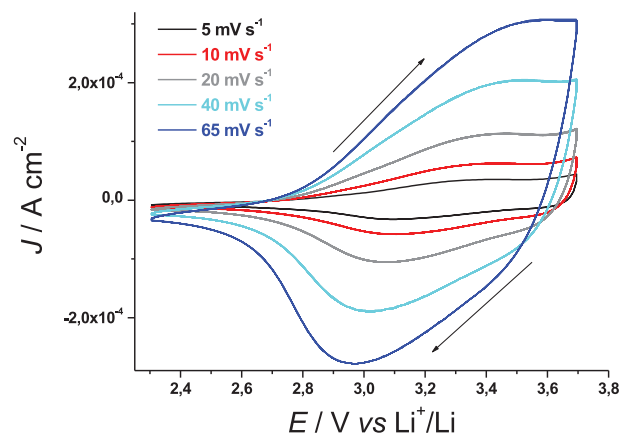

Fig. 28. Effect on the scan rate on the voltammogram of the RDS NiO sample shown in Fig. 25. The curves were recorded after reaching a stable voltammogram for the NiO layer at 5 mV s^{-1}. For electrolyte used see Fig. 26.
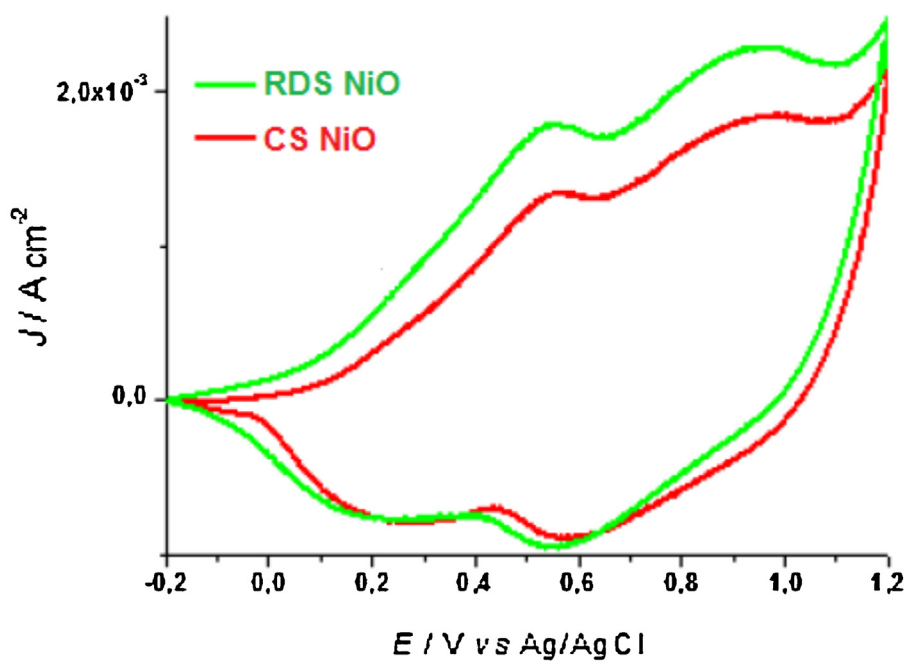Adapted from Ref. [45].

Fig. 29. Effect of the sintering method on the voltammogram of mesoporous NiO samples prepared via CS and RDS of 50 nm diameter NiO nanoparticles. Scan rate: 40 mV s^{-1}; aqueous electrolyte as in Figure 27.
Adapted from Ref. [47].

implies also an increase of its charge capacitance due to the uptake of ions that are required to compensate the charge acquired by NiO during the redox process [54]. The simultaneous uptake/release of electrons and ions (Eqs. (1)–(5)) has important consequences also on the overall conductivity of NiO, a system representing a mixed conductor with both electrons (or holes) and ions acting as charge carriers in the oxidized/reduced (or p-doped/n-doped) forms [120]. An analysis of the variations in charge transport kinetics, capacitance, density of states above valence band upper edge, and electron/ionic diffusivity of oxidized/reduced NiO thin films upon application of an external bias was carried out using electrochemical impedance spectroscopy (EIS) [92,103,121]. The EI spectra of NiO [44,104,106] are characterized by a high-frequency semicircle that represents the parallel combination of a resistance and a capacitance associated generally with the process of charge transfer at the NiO/electrolyte interface. This feature is scarcely affected by the potential value in the range of NiO oxidation, and is followed by linear tracts with variable slope upon decrease of the frequency of stimulus (Figs. 30 and 31). When the linear portion of the EI spectrum has a slope of 45° the oxide enters in a regime of charge diffusion with the charges moving at those frequencies either within the structure of the oxide [104] or through the pores of the nanostructured oxide [122]. In this regime, the diffusive motions of ions and electronic carriers in oxidized NiO are no longer independent due to the field effects exerted by one kind of charge carrier to the other [123]. Upon further decrease of the frequency of stimulus the spectra of oxidized NiO (Figs. 30 and 31) tend to further increase their slope till they reach a quasi-vertical trend that is indicative of a limiting capacitive behaviour [106]. Since both oxidation (Eqs. (1) and (2)) and reduction (Eq. (3)) processes in NiO involve the uptake of anions and cations, respectively, the spectra of reduced NiO will present analogous features with those of oxidized NiO with the appearance of diffusive and capacitive features [96]. The equivalent Randles-type circuit shown in Fig. 32 [124,125] has been proposed as a model for the description of the impedance spectra in reduced and oxidized NiO, and values of diffusivity in the order of 10^{-11} cm^2 s^{-1} have been found for lithium intercalated samples of reduced NiO (Eq. (3)) [44,104,106].

The analysis of the electrochemical properties of NiO has been extended also to sensitized NiO samples [44,46,47]. The motivation for such a study is the investigation of possible charge transfer processes between oxidized NiO and the chemisorbed dye in the absence of the redox shuttle under both in the dark [46,47] and illuminated conditions [44]. The main effect of dye-sensitization upon the electrochemical properties of NiO as far as oxidation is concerned, i.e. in the condition of electrochemical hole injection, is the passivation of the oxide surface with a general decrease of the current density in passing from the bare to the sensitized state. In fact, not every portion of the surface of NiO is modified upon sensitization with the consequence that some parts of NiO surface still remain in the bare state even after prolonged sensitization. Since NiO oxidation takes place on the unsensitized portions of NiO surface, the dye apparently prevents the surface confined oxidation of NiO [46,47]. The resulting inhibiting effect of sensitization on the oxidation of NiO$_x$ is similar to what occurs in Li-doped NiO. However, there is a difference in the cause of such an effect: sensitization acts on the kinetics of NiO$_x$ oxidation by slowing down the process of electrochemical formation of holes, whereas p-doping with lithium cations shifts the energetics of the process at larger oxidation potential [103].

NiO bound sensitizers analyzed so far did not present evidence for dye-based redox processes within the potential range of the oxidation of NiO. This was confirmed by the absence additional redox peaks in the voltammograms of sensitized NiO with erythrosine and P1 dyes. Repetitive cycling of erythrosine-sensitized NiO in anhydrous electrolyte showed features of activation of a NiO-based oxidation that is surface based (Fig. 33) as in the case of the bare oxide (Fig. 25), with a oxidation current that was proportional to the scan rate in a linear fashion (vide supra) (Fig. 34) [44].

Recently, the oxidation of a squaraine-based sensitizer immobilized on nanostructured NiO and polarized within the oxidation range of NiO has been reported. This process led to the detachment of the dye from the supporting oxide with the recovery of the electrochemical features of bare NiO [126]. In the absence of any redox shuttle in the electrolyte, NiO sensitized with erythrosine is photoconductive as shown by the increase of the oxidation
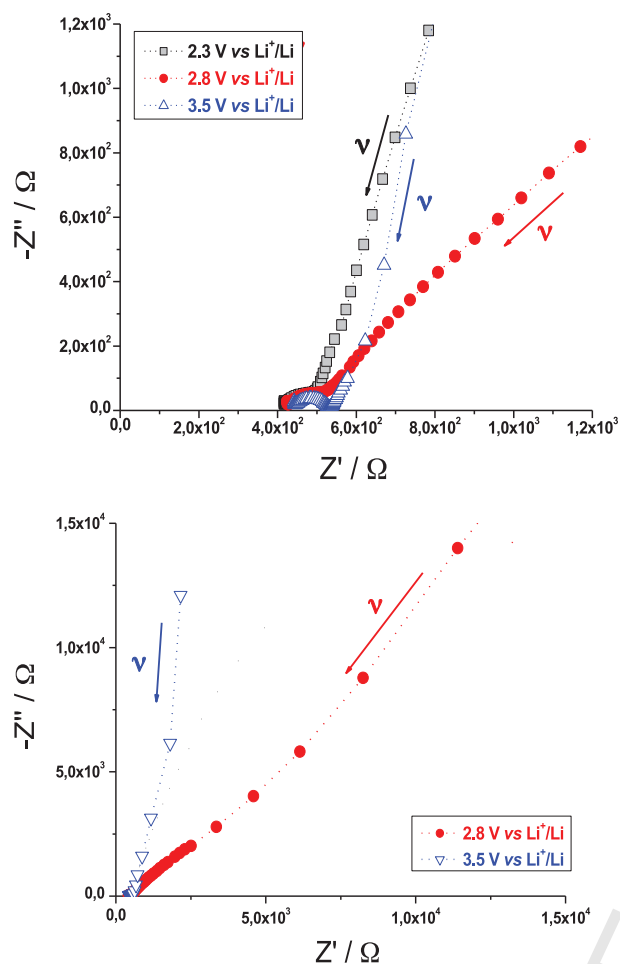
Fig. 32. Equivalent circuit modelling of the electrochemical behaviour of fully oxidized NiO_x at 3.55 V vs. Li^+/Li (see Fig. 31). C_{DL} = capacitance of the double layer at the NiO electrode/electrolyte interface; R_{CT} = charge transfer resistance through NiO_x electrode/electrolyte interface; Z_w = Warburg impedance associated with charge transport through NiO_x electrode; C_L = limiting capacitance due to the finite thickness of NiO_x film.

For further details see Ref. [105].

Fig. 33. Evolution of the voltammogram of erythrosine-sensitized NiO at 5 mV s^{-1} in dark conditions upon continuous cycling of type of NiO sample as shown in Fig. 25. For electrolyte used see Fig. 26.

Adapted from Ref. [45].

Fig. 30. (top) High- and (bottom) low-frequency EI spectra of RDS NiO (l = 0.4 µm) deposited onto ITO at different applied potentials (E_{appl}). The selected values of E_{appl} are related to the nature of the NiO layer, in the pristine state [E_{appl} = 2.3 V vs. Li^+/Li, open circuit voltage], in the partially oxidized state (E_{appl} = 2.8 V vs. Li^+/Li) and in the fully oxidized state (E_{appl} = 3.5 V vs. Li^+/Li). For electrolyte used see Fig. 26.
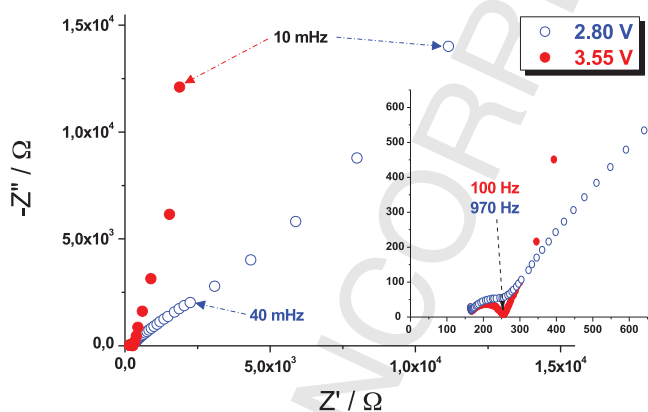
Graph adapted from Ref. [45].

Fig. 31. EIS profiles of NiO_x sintered via CS at different applied potentials (2.8 and 3.55 V vs. Li^+/Li). In the larger Picture 40 mHz marks the onset of the diffusive regime in NiO when is polarized at 2.8 V. In the inset the specified frequencies refer to the point of closure of the high-frequencies semicircles. NiO_x film thickness: 0.3 µm. For electrolyte used see Fig. 26.
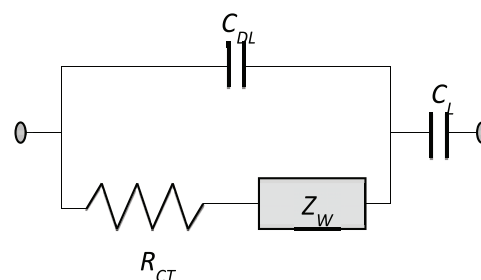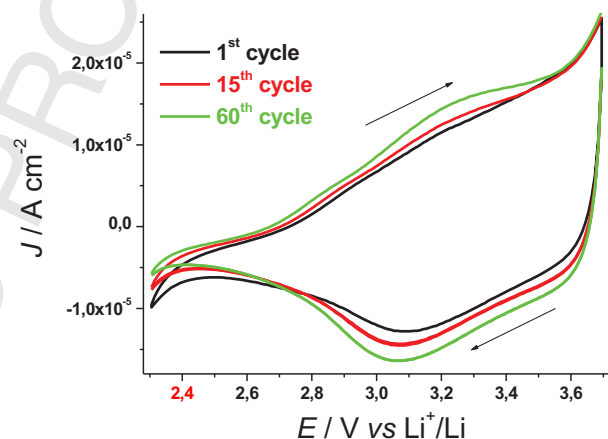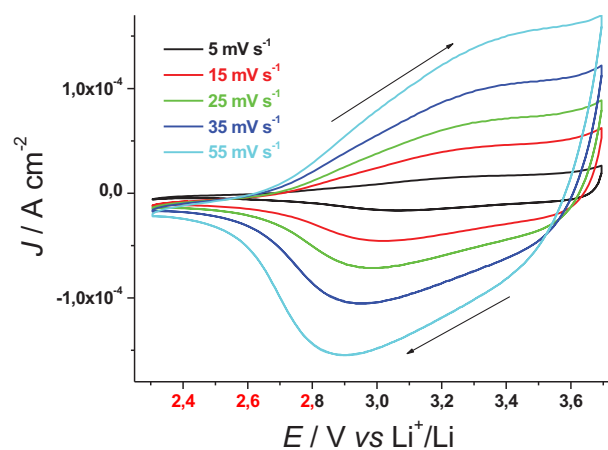
Adapted from Ref. [45].

Fig. 34. Effect on the scan rate on the voltammogram of erythrosine-sensitized NiO sample as shown in Fig. 33. The cyclic voltammograms were recorded after reaching stabilization of the voltammogram of erythrosine-sensitized NiO at 5 mV s^{-1}. For electrolyte used see Fig. 26.
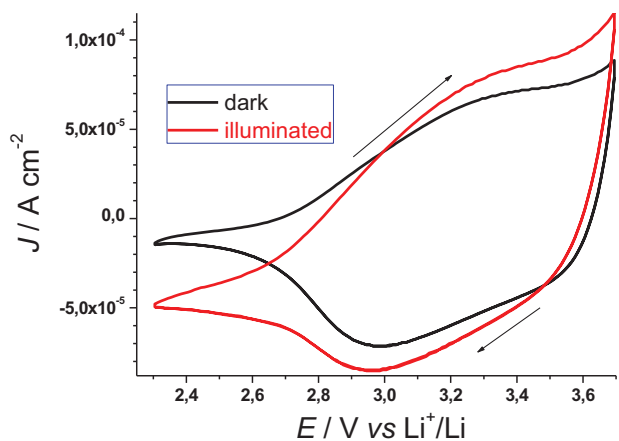
Adapted from Ref. [45].

Fig. 35. Effect of white light illumination (I_{in}: 25 W cm^{-2}) on the oxidation of NiO when the oxide is sensitized with erythrosine. The cyclic voltammograms were recorded at 25 mV s^{-1}. For electrolyte used see Fig. 26.
Adapted from Ref. [45].

current in passing from the dark to the illuminated state. At the basis of the photoeffect is the increase of the number of Ni(III) centres induced by the sensitization of NiO with erythrosine with consequent favouring of the oxidation process of Eq. (1) (Fig. 35). The kinetics of the electrochemical oxidation of sensitized NiO under illumination is controlled by the same factor as for dark oxidation. This was confirmed by the observation of a linear trend between the current density and the scan rate both under illumination and in dark conditions (Fig. 36).

Importantly, photoconductivity effects could not be observed in bare mesoporous NiO when oxidation was carried out under anhydrous conditions (Eqs. (1) and (2)) [47] whereas bare NiO displayed weak photoconductivity effects during reduction (Eq. (3)) [95]. Since this photoconductivity effect was more evident during the reduction process of NiO rather than that of its oxidation [113], it was concluded that the variations of optical transmission occurring in reduced NiO are more effective in producing photo-effects with respect to oxidized NiO [104,127].

The effect of sensitization on the electrochemical reduction of NiO was studied when erythrosine was the dye-sensitizer [95]. The redox peaks originated from dye-based electrochemical processes could be detected in the return scan whereas the signal of the reduction of NiO overlapped with that of the dye in the forward
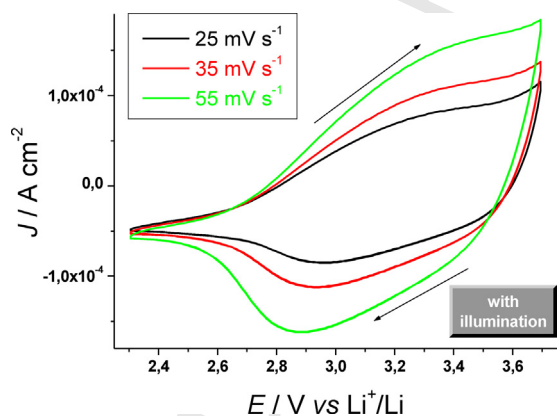

Fig. 36. Scan rate dependence of the voltammogram of erythrosine-sensitized NiO at 5 mV s^{-1} under illumination with white light (I_{in}: 25 W cm^{-2}). Voltammograms were recorded after stabilization of the voltammogram obtained at 5 mV s^{-1}. For electrolyte used see Fig. 26.
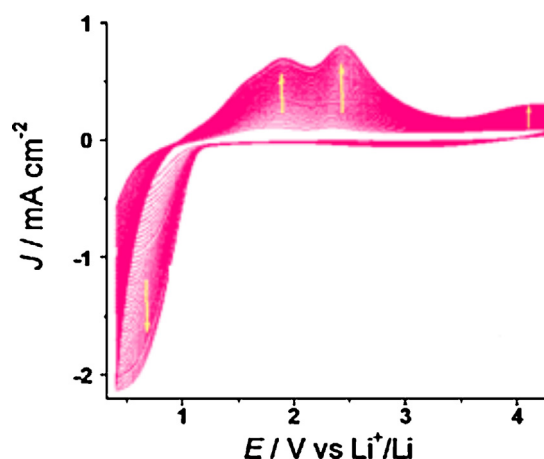Adapted from Ref. [45].

Fig. 37. Cyclic voltammograms of erythrosine-sensitized NiO with a thickness of 1.2 μm. Electrolyte: 0.5 M LiClO$_4$ in anhydrous propylene carbonate; scan rate: 40 mV s^{-1}. Yellow arrows show the direction of variation of the various current peaks with cycling.
Adapted from Ref. [97].

scan (Fig. 37). The nature of the electrochemical processes occurring during the reduction of erythrosine–sensitized NiO remains still unclear.

The electrochemical properties of thin nickel oxide films discussed above show how these films can undergo oxidation and reduction processes that alter its electrical conductivity and its capability of storing charge. These processes introduce features in the oxide, which are typical of mixed conductors with both ionic and electronic charge carriers. The kinetics of NiO oxidation and reduction are controlled either by a surface confined electron transfer process or by the diffusion of charge carriers within the oxide depending on the chemical composition of the oxide, its porosity, the crystal structure and the nature of the electrolyte. In the framework of DSC research, the electrochemical properties of mesoporous NiO in both bare and dyed states are of particular interest since the dark oxidation of NiO corresponds to electrochemical hole injection and give clues about the intrinsic stability and mobility of the injected hole in the oxide under conditions when no recombination with the redox shuttle can take place. A correlation between the electrochemical properties of NiO in the absence of redox shuttles, and the photoelectrochemical properties of sensitized NiO in p-type DSCs is desired because of the crucial role of the hole transport phenomena through the oxide. This aspect still needs to be investigated in a systematic way and, in this respect, the analysis of the electrochemical properties of mesoporous NiO (either bare or sensitized) can be of great usefulness especially when different NiO samples for DSCs have to be compared.

6. Concluding remarks

The electrochemistry of nickel oxide thin films is complex because of the bipolar nature of this system that can undergo both electrochemical oxidation (p-doping) and reduction (n-doping) in a reversible manner. This has important consequences for oxide conductivity, density of states distribution, charge transfer properties, optical absorption, photoconductivity and photoelectrochemical properties, depending on the potential of polarization at which the electrochemical doping of nickel oxide is conducted. The extent of electrochemical oxidation/reduction in nickel oxide films can be controlled through a variety of electrochemical conditions, e.g. potentiostatic, potentiodynamic and galvanostatic, which make possible the fine modulation of all the properties of nickel oxide which are influenced by the electronic structure of the material. The

oxidation of NiO_x is characterized by having a surface confinement as determined by the analysis of cyclic voltammetry data at variable scan rate and by the direct proportionality between current density and geometrical area in nanoporous samples. This holds also when NiO_x is in a sensitized state the dye-sensitizers being those of common use in p-type DSCs with I_3^-/I^- as redox shuttle. For this reason surface morphology is of primary importance to control the oxidation properties of NiO_x. The reduction of NiO_x has been studied extensively for the evaluation of the capacitive properties as far as capacitors, lithium battery electrodes and electrochromic devices were concerned. Van der Waals characteristics as well as crystalline phase play a major role in the control of the cathodic properties of nickel oxide since the solid state reduction of NiO_x implies the occurrence of topotactic processes like cation intercalation and ion diffusion within oxide structure and between Van Der Waals planes. By virtue of this combination of electrochemical characteristics the corresponding electrocatalytic properties of NiO_x can be also varied in an opportune fashion. In the framework of p-DSCs it has been observed that the oxidation of NiO_x (i.e. the electrochemical injection of holes) triggers the oxidation of iodide and acts as an electrocatalytic layer with respect to the underlying conductive substrate made of a TCO. Iodide oxidation corresponds to the deleterious process of charge recombination and limits seriously the conversion efficiency in NiO-based p-DSCs. To avoid that some authors have considered the chemical doping of the oxide film with the cations derived from the elements of the first group (mostly lithium cations) as doping agents of p-type. The p-type conductivity of the doped oxide increased with respect to its pristine version and the Fermi level was shifted to mismatch the energy levels of the empty electroactive states with those of the redox shuttle.

It is difficult to judge what is the "ideal" preparation method for NiO for use in p-type dye-sensitized solar cells. Improving the charge transport time in the electrodes is an important requirement, but NiO is not as versatile as some n-type materials such as ZnO in terms of modifying the morphology. However, in addition to the typical cubic nanocrystals, rods have now been prepared. Clearly, the presence of defects is important to the performance of the device, especially the recombination reactions. The issues of film thickness and adhesion appear to have mostly been solved in recent publications. However, one of the limiting properties of NiO is the colouration, particularly when thicker films are used. A degree of scattering is positive in terms of improving light harvesting but is problematic for physical chemists wishing to investigate the photoinduced charge-transfer reactions spectroscopically. The most efficient devices have been prepared from pre-formed NiO nanoparticles. Control over the purity and crystallinity is achieved by preparing the particles in house. In terms of deposition, screen printing provides a reproducible route that is suitable for scale-up, but spray deposition avoids the requirement for organic binders that need to be burned off. One of the most exciting developments is the opportunity to sinter the particles in a microwave, which significantly reduces the time required and energy input. More work is now needed to understand the reasons for the low fill factor in these devices, including the apparent "photo shunt" so that the properties of the NiO can be improved accordingly.

Q9 References

[1] J. He, H. Lindström, A. Hagfeldt, S. Lindquist, Sol. Energy Mater. Sol. Cells 62 (2000) 265.
[2] A. Nattestad, A.J. Mozer, M.K.R. Fischer, Y.-B. Cheng, A. Mishra, P. Bäuerle, U. Bach, Nat. Mater. 9 (2010) 31.
[3] E.A. Gibson, A.L. Smeigh, L. Le Pleux, J. Fortage, G. Boschloo, E. Blart, L. Hammarström, Angew. Chem. Int. Ed. 48 (2009) 4402.
[4] A. Nakasa, H. Usami, S. Sumikura, S. Hasegawa, T. Koyama, E. Suzuki, Chem. Lett. 34 (2005) 500.
[5] S. Mathew, A. Yella, P. Gao, R. Humphry-Baker, B.F.E. Curchod, N. Ashari-Astani, I. Tavernelli, U. Rothlisberger, Md.K. Nazeeruddin, M. Grätzel, Nat. Chem. 6 (2014) 242.
[6] C.J. Wood, G.H. Summers, E.A. Gibson, Chem. Commun. (2015), http://dx.doi.org/10.1039/C4CC10230D
[7] S. Powar, T. Daeneke, M.T. Ma, D. Fu, N.W. Duffy, G. Goetz, M. Weidelener, A. Mishra, P. Baeuerle, L. Spiccia, U. Bach, Angew. Chem. Int. Ed. 52 (2013) 602.
[8] F. Odobel, Y. Pellegrin, E.A. Gibson, A. Hagfeldt, A.L. Smeigh, L. Hammarström, Coord. Chem. Rev. 256 (2012) 2414.
[9] L. Li, E.A. Gibson, P. Qin, G. Boschloo, M. Gorlov, A. Hagfeldt, L. Sun, Adv. Mater. 22 (2010) 1759.
[10] S. Mori, S. Fukuda, S. Sumikura, J. Phys. Chem. C 112 (2008) 16134.
[11] A. Morandeira, J. Fortage, T. Edvinsson, L. Le Pleux, E. Blart, G. Boschloo, F. Odobel, J. Phys. Chem. C 112 (2008) 1721.
[12] S. Powar, Q. Wu, M. Weidelener, A. Nattestad, Z. Hu, A. Mishra, P. Bäuerle, L. Spiccia, Y.B. Cheng, U. Bach, Energy Environ. Sci. 5 (2012) 8896.
[13] A. Hagfeldt, G. Boschloo, L. Sun, L. Kloo, H. Pettersson, Chem. Rev. 110 (2010) 6595.
[14] Z. Liu, W. Li, S. Topa, X. Xu, X. Zeng, Z. Zhao, M. Wang, W. Chen, F. Wang, Y.-B. Cheng, H. He, ACS Appl. Mater. Interfaces 6 (2014) 10614.
[15] H.-T. Wang, D.K. Mishra, P. Chen, J.-M. Ting, J. Alloys Compd. 584 (2014) 142.
[16] L. Le Pleux, A.L. Smeigh, E. Gibson, Y. Pellegrin, E. Blart, G. Boschloo, A. Hagfeldt, L. Hammarström, F. Odobel, Energy Environ. Sci. 4 (2011) 2075.
[17] L. Zhu, H. Yang, C. Zhong, C. Li, Chem. Asian J. 7 (2012) 2791.
[18] G. Natu, Z. Huang, Z. Ji, Y. Wu, Langmuir 28 (2012) 950.
[19] Y. Mizoguchi, S. Fujihara, Electrochem. Solid-State Lett. 11 (2008) K78.
[20] H.B. Yang, B. Liu, S.Y. Khoo, L.N. Zhu, C.X. Guo, Y.Q. Dong, C.M. Li, Adv. Mater. Interfaces 1 (2014) 13000110.
[21] H. Yang, G.H. Guai, C. Guo, Q. Song, S.P. Jiang, Y. Wang, W. Zhang, C.M. Li, J. Phys. Chem. C 115 (2011) 12209.
[22] P. Qin, M. Linder, T. Brinck, G. Boschloo, A. Hagfeldt, L.C. Sun, Adv. Mater. 21 (2009) 2993.
[23] J. He, H. Lindström, A. Hagfeldt, S.-E. Lindquist, J. Phys. Chem. B 103 (1999) 8940.
[24] H. Zhu, A. Hagfeldt, G. Boschloo, J. Phys. Chem. C 111 (2007) 17455.
[25] C.J. Flynn, E.E. Oh, S.M. McCullough, R.W. Call, C.L. Donley, R. Lopez, J.F. Cahoon, J. Phys. Chem. 118 (2014) 14177.
[26] P. Qin, H. Zhu, T. Edvinsson, G. Boschloo, A. Hagfeldt, L. Sun, J. Am. Chem. Soc. 130 (2008) 8570.
[27] T. Brinck, G. Boschloo, A. Hagfeldt, L. Sun, Adv. Mater. 21 (2009) 2993.
[28] L. Le Pleux, B. Chavillon, Y. Pellegrin, E. Blart, L. Cario, S. Jobic, F. Odobel, Inorg. Chem. 48 (2009) 8245.
[29] K.-J. Hwang, S.-J. Yoo, S.-H. Jung, D.-W. Park, S.-I. Kim, J.-W. Lee, Bull. Korean Chem. Soc. 30 (2009) 172.
[30] Q. Wu, Y.S.L. Li, M. Cao, F. Gu, L. Wang, Appl. Surf. Sci. 276 (2013) 411.
[31] Y. Qu, W. Zhou, X. Miao, Y. Li, L. Jiang, K. Pan, G. Tian, Z. Ren, G. Wang, H. Fu, Chem. Asian J. 8 (2013) 3085.
[32] A. Renaud, B. Chavillon, L. Cario, L. Le Pleux, N. Szuwarski, Y. Pellegrin, E. Blart, E. Gautron, F. Odobel, S. Jobic, J. Phys. Chem. C 117 (2013) 22478.
[33] N. Tsuda, K. Nasu, A. Fujimori, K. Siratori, Electronic Conduction in Oxides, 2nd ed., Springer, Berlin, Germany, 2000.
[34] P. Monk, R. Mortimer, D. D. Rosseinsky, Electrochromism and Electrochromic Devices, Cambridge University Press, Cambridge, 2007.
[35] G.A. Niklasson, C.G. Granqvist, J. Mater. Chem. 17 (2007) 127.
[36] R. Newman, R. Chrenko, Phys. Rev. 114 (1959) 1507.
[37] G. Boschloo, A. Hagfeldt, J. Phys. Chem. B 105 (2001) 3039.
[38] L.E. Smart, E.A. Moore, Solid State Chemistry, 3rd ed., Taylor Francis, 2005.
[39] H.C. Kim, S.M. Park, W.D. Hinsberg, Chem. Rev. 110 (2010) 146.
[40] P. Yang, D. Zhao, D.I. Margolese, B.F. Chmelka, G.D. Stucky, Chem. Mater. 11 (1999) 2813.
[41] S. Sumikura, S. Mori, S. Shimizu, H. Usami, E. Suzuki, J. Photochem. Photobiol. A 199 (2008) 1.
[42] M. Bräutigam, M. Schulz, J. Inglis, J. Popp, J.G. Vos, B. Dietzek, Phys. Chem. Chem. Phys. 14 (2012) 15185.
[43] M. Bräutigam, P. Weyell, T. Rudolph, J. Dellith, S. Krieck, H. Schmalz, F.H. Schacher, B. Dietzek, J. Mater. Chem. A 2 (2014) 6158.
[44] M. Awais, D.P. Dowling, M. Rahman, J.G. Vos, F. Decker, D. Dini, J. Appl. Electrochem. 43 (2013) 191.
[45] A. Nattestad, M. Ferguson, R. Kerr, Y.-B. Cheng, U. Bach, Nanotechnology 19 (2008) 295.
[46] E.A. Gibson, M. Awais, D. Dini, D.P. Dowling, M.T. Pryce, J.G. Vos, G. Boschloo, A. Hagfeldt, Phys. Chem. Chem. Phys. 15 (2013) 2411.
[47] M. Awais, E.A. Gibson, J.G. Vos, D.P. Dowling, A. Hagfeldt, D. Dini, ChemElectroChem 2 (2014) 384.
[48] A. Hagfeldt, U.B. Cappel, G. Boschloo, L. Sun, L. Kloo, H. Pettersson, E.A. Gibson, in: A. McEvoy, T. Markvart, L. Castaner (Eds.), Practical Handbook of Photovoltaics: Fundamentals and Applications, 2nd ed., Elsevier, 2012.
[49] K.A. Click, D.R. Beauchamp, B.R. Garrett, Z. Huang, C.M. Hadad, Y. Wu, Phys. Chem. Chem. Phys. 16 (2014) 26103.
[50] J.L. Segura, H. Herrera, P. Bäuerle, J. Mater. Chem. 22 (2012) 8717.
[51] X.L. Zhang, Z. Zhang, D. Chen, P. Bäuerle, U. Bach, Y.-B. Cheng, Chem. Commun. 48 (2012) 9885.
[52] C.J. Barbe, F. Arendse, P. Comte, M. Jirousek, F. Lenzmann, V. Shklover, M. Grätzel, J. Am. Ceram. Soc. 80 (1997) 3157.
[53] X.L. Zhang, Z. Zhang, F. Huang, P. Bäuerle, U. Bach, Y.-B. Cheng, J. Mater. Chem. 22 (2012) 7005.

[54] M.S. Wu, M.J. Wang, Chem. Commun. 46 (2010) 6968.
[55] G. Fu, Y. Hu, L. Xie, X. Jin, Y. Xie, Y. Wang, Z. Zhang, Y. Yang, H. Wu, Int. J. Electrochem. Sci. 4 (2009) 1052.
[56] H. Wang, Q. Pan, X. Wang, G. Yin, J. Zhao, J. Appl. Electrochem. 39 (2009) 1597.
[57] Y.Y. Xi, D. Li, A.B. Djurišić, M.H. Xie, K.Y.K. Man, W.K. Chan, Electrochem. Solid-State Lett. 11 (2008) D56.
[58] K.W. Nam, K.B. Kim, J. Electrochem. Soc. 149 (2002) A346.
[59] M. Tachiki, T. Hosomi, T. Kobayashi, Jpn. J. Appl. Phys. 39 (2000) 1817.
[60] Y. Kakehi, S. Nakao, K. Satoh, T. Kusaka, J. Cryst. Growth 237 (2002) 591.
[61] V. Verma, M. Katiyar, Thin Sol. Films 527 (2013) 369.
[62] E. Fujii, A. Tomozawa, S. Fujii, H. Torii, M. Hattori, R. Takayama, Jpn. J. Appl. Phys. 32 (1993) L1448.
[63] L. Berkat, L. Cattin, A. Reguig, M. Regragui, J.C. Bernede, Mater. Chem. Phys. 89 (2005) 11.
[64] X.H. Xia, J.P. Tu, J. Zhang, X.L. Wang, W.K. Zhang, H. Huang, Electrochim. Acta 53 (2008) 5721.
[65] H. Huang, J. Tian, W.K. Zhang, Y.P. Gan, X.Y. Tao, X.H. Xia, J.P. Tu, Electrochim. Acta 56 (2011) 4281.
[66] C.G. Granqvist, Adv. Mater. 15 (2003) 1789.
[67] S. Ito, P. Chen, P. Comte, Md.K. Nazeeruddin, P. Liska, P. Péchy, M. Grätzel, Prog. Photovolt.: Res. Appl. 15 (2007) 603.
[68] Z. Huang, G. Natu, Z. Ji, M. He, M. Yu, Y. Wu, J. Phys. Chem. C 116 (2012) 26239.
[69] L.M. Peter, Phys. Chem. Chem. Phys. 9 (2007) 2630.
[70] L.M. Peter, J. Electroanal. Chem. 599 (2007) 233.
[71] M. Miyashita, K. Sunahara, T. Nishikawa, Y. Uemura, N. Koumura, K. Hara, S. Mori, J. Am. Chem. Soc. 130 (2008) 17874.
[72] G. Natu, P. Hasin, Z. Huang, Z. Ji, M. Fe, Y. Wu, ACS Appl. Mater. Interfaces 4 (2012) 5922.
[73] A. Morandeira, G. Boschloo, A. Hagfeldt, L. Hammarström, J. Phys. Chem. B 109 (2005) 19403.
[74] A.L. Smeigh, L. Le Pleux, J. Fortage, Y. Pellegrin, E. Blart, F. Odobel, L. Hammarström, Chem. Commun. 48 (2012) 678.
[75] X. Wu, G. Xing, S.L.J. Tan, R.D. Webster, T.C. Sum, E.K.L. Yeow, Phys. Chem. Chem. Phys. 14 (2012) 9511.
[76] T.W. Hamann, O.K. Farha, J.T. Hupp, J. Phys. Chem. C 112 (2008) 19756.
[77] B.A. Gregg, F. Pichot, S. Ferrere, C.L. Fields, J. Phys. Chem. B 105 (2001) 1422.
[78] E. Palomares, J.N. Clifford, S.A. Haque, T. Lutz, J.R. Durrant, J. Am. Chem. Soc. 125 (2003) 475.
[79] S. Uehara, S. Sumikura, E. Suzuki, S. Mori, Energy Environ. Sci. 3 (2010) 641.
[80] Z. Bian, T. Tachikawa, S.-C. Cui, M. Fujitsuka, T. Majima, Chem. Sci. 3 (2012) 370.
[81] E. Thimsen, A.B.F. Martinson, J.W. Elam, M.J. Pellin, J. Phys. Chem. C 116 (2012) 16830.
[82] K.V. Rao, A. Smakula, J. Appl. Phys. 36 (1965) 2031.
[83] J.A. Anta, E. Guillen, R. Tena-Zaera, J. Phys. Chem. C 116 (2012) 11413.
[84] C.G. Granqvist, Sol. Energy Mater. Sol. Cells 99 (2012) 1.
[85] X. Wang, L. Qiao, X. Sun, X. Li, D. Hu, Q. Zhang, D. He, J. Mater. Chem. A 1 (2013) 4173.
[86] F. Vera, R. Schrebler, E. Munoz, C. Suarez, P. Cury, H. Gomez, R. Cordova, R. Marotti, E. Dalchiele, Thin Solid Films 490 (2005) 182.
[87] W. Estrada, A.M. Andersson, C.G. Granqvist, A. Gorenstein, F. Decker, J. Mater. Res. 6 (1991) 1715.
[88] C.G. Granqvist, Solid State Ion. 53–56 (1992) 479.
[89] C.G. Granqvist, Sol. Energy Mater. Sol. Cells 91 (2007) 1529.
[90] D. Adler, J. Feinleib, Phys. Rev. B 2 (1970) 3112.
[91] M. Nachman, L.N. Cojocaru, L.V. Ribco, Phys. Status Solidi B 8 (1965) 773.
[92] L. D'Amario, G. Boschloo, A. Hagfeldt, L. Hammarström, J. Phys. Chem. C 118 (2014) 19556.
[93] P. Calka, E. Martinez, D. Lafond, S. Minoret, S. Tirano, B. Detlefs, J. Roy, J. Zegenhagen, C. Guedj, J. Appl. Phys. 109 (2011) 124507.
[94] M. Awais, M. Rahman, J.M. Don McElroy, D. Dini, J.G. Vos, D.P. Dowling, Surf. Coat. Technol. 205 (2011) S245.
[95] M. Awais, D. Dini, J.M. Don McElroy, Y. Halpin, J.G. Vos, D.P. Dowling, J. Electroanal. Chem. 689 (2013) 185.
[96] M. Awais, M. Rahman, J.M. Don McElroy, N. Coburn, D. Dini, J.G. Vos, D.P. Dowling, Surf. Coat. Technol. 204 (2010) 2729.
[97] X.L. Zhang, F. Huang, A. Nattestad, K. Wang, D. Fu, A. Mishra, P. Bäuerle, U. Bach, Y.B. Cheng, Chem. Commun. 47 (2011) 4808.
[98] F.A. Cotton, G. Wilkinson, Advanced Inorganic Chemistry, 5th ed., John Wiley, New York, 1988, pp. 743.
[99] P.S. Aggarwal, A. Goswami, J. Phys. Chem. 65 (1961) 2105.
[100] A.G. Marrani, V. Novelli, S. Sheehan, D.P. Dowling, D. Dini, ACS Appl. Mater. Interfaces 6 (2014) 143.
[101] V.O. Williams, E.J. De Marco, M.J. Katz, J.A. Libera, S.C. Riha, D.W. Kim, J.R. Avila, A.B.F. Martinson, J.W. Elam, M.J. Pellin, O.K. Farha, J.T. Hupp, ACS Appl. Mater. Interfaces 6 (2014) 12290.
[102] M. Gong, W. Zhou, M.C. Tsai, J. Zhou, M. Guan, M.C. Lin, B. Zhang, Y. Hu, D.Y. Wang, J. Yang, S.J. Pennycook, B.J. Hwang, H. Dai, Nat. Commun. 5 (2014) 4695.
[103] T.A. Nirmal Peiris, J.S. Sagu, K.G. upul Wijayantha, J. Garcia-Cañadas, ACS Appl. Mater. Interfaces 6 (2014) 14988.
[104] S. Passerini, B. Scrosati, J. Electrochem. Soc. 141 (1994) 889.
[105] S. Passerini, J. Scarminio, B. Scrosati, D. Zane, F. Decker, J. Appl. Electrochem. 23 (1993) 1187.
[106] F. Decker, S. Passerini, R. Pileggi, B. Scrosati, Electrochim. Acta 37 (1992) 1033.
[107] M.E.G. Lyons, L. Russell, M. O'Brien, R.L. Doyle, I. Godwin, M.P. Brandon, Int. J. Electrochem. Sci. 7 (2012) 2710.
[108] S. Hüfner, T. Riesterer, Phys. Rev. B 33 (1986) 7267.
[109] H. Gerischer, Electrochim. Acta 35 (1990) 1677.
[110] W.P. Gomes, F. Cardon, Prog. Surf. Sci. 12 (1982) 155.
[111] S. Sheehan, G. Naponiello, F. Odobel, D.P. Dowling, A. Di Carlo, D. Dini, J. Solid State Electrochem. (2015). http://dx.doi.org/10.1007/s10008-014-2703-9
[112] E. Avendano, H. Rensmo, A. Azens, A. Sandell, G.M. Azevedo, H. Siegbahn, G.A. Niklasson, C.G. Granqvist, J. Electrochem. Soc. 156 (2009) P132.
[113] V. Novelli, M. Awais, D.P. Dowling, D. Dini, Am. J. Anal. Chem. 6 (2015) 176.
[114] H. Bode, K. Dehmelt, J. Witte, Electrochim. Acta 11 (1966) 1079.
[115] D. Yohe, A. Riga, R. Greef, E. Yeager, Electrochim. Acta 13 (1968) 1351.
[116] R. Schöllhorn, Physica B 99 (1980) 89.
[117] D. Dini, F. Decker, Electrochim. Acta 43 (1998) 2919.
[118] H. Gerischer, F. Decker, B. Scrosati, J. Electrochem. Soc. 141 (1994) 2297.
[119] J. Bard, L.R. Faulkner, Electrochemical Methods, Fundamental and Application, John Wiley & Sons, New York, 1980.
[120] D. Cahen, K. Gartsman, ISSI Lett. 3 (1993) 10.
[121] J.R. MacDonald, Electrochim. Acta 35 (1990) 1483.
[122] S.K. Meher, P. Justin, G.R. Rao, Electrochim. Acta 55 (2010) 8388.
[123] R.P. Buck, J. Electroanal. Chem. 271 (1989) 1.
[124] R.P. Buck, Electrochim. Acta 35 (1990) 1509.
[125] M. Sluyters-Rehbach, Pure Appl. Chem. 66 (1994) 1831.
[126] Prof. Franco Decker (Dept. of Chemistry, University of Rome "La Sapienza"), private communication.
[127] S. Green, J. Backolm, P. Georen, C.G. Granqvist, G.A. Niklasson, Sol. Energy Mater. Sol. Cells 93 (2009) 2050.